

# Finite-frequency sensitivity of body waves to anisotropy based upon adjoint methods

Anne Sieminski,<sup>1</sup> Qinya Liu,<sup>2</sup> Jeannot Trampert<sup>1</sup> and Jeroen Tromp<sup>2</sup>

<sup>1</sup>Department of Earth Sciences, Utrecht University, PO Box 80021, TA 3058 Utrecht, the Netherlands. E-mail: anne@geo.uu.nl

<sup>2</sup>Seismological Laboratory, California Institute of Technology, Pasadena, CA 91125, USA

Accepted 2007 June 20. Received 2007 June 15; in original form 2007 March 19

## SUMMARY

We investigate the sensitivity of finite-frequency body-wave observables to mantle anisotropy based upon kernels calculated by combining adjoint methods and spectral-element modelling of seismic wave propagation. Anisotropy is described by 21 density-normalized elastic parameters naturally involved in asymptotic wave propagation in weakly anisotropic media. In a 1-D reference model, body-wave sensitivity to anisotropy is characterized by ‘banana–doughnut’ kernels which exhibit large, path-dependent variations and even sign changes. *P*-wave travel-times appear much more sensitive to certain azimuthally anisotropic parameters than to the usual isotropic parameters, suggesting that isotropic *P*-wave tomography could be significantly biased by coherent anisotropic structures, such as slabs. Because of shear-wave splitting, the common cross-correlation traveltime anomaly is not an appropriate observable for *S* waves propagating in anisotropic media. We propose two new observables for shear waves. The first observable is a generalized cross-correlation traveltime anomaly, and the second a generalized ‘splitting intensity’. Like *P* waves, *S* waves analysed based upon these observables are generally sensitive to a large number of the 21 anisotropic parameters and show significant path-dependent variations. The specific path-geometry of *SKS* waves results in favourable properties for imaging based upon the splitting intensity, because it is sensitive to a smaller number of anisotropic parameters, and the region which is sampled is mainly limited to the upper mantle beneath the receiver.

**Key words:** adjoint methods, body waves, Fréchet derivatives, seismic anisotropy, sensitivity, shear-wave splitting.

## 1 INTRODUCTION

Seismic anisotropy is an essential property of the elastic structure of the mantle. Many mantle minerals are anisotropic (Mainprice *et al.* 2000) and can be preferentially oriented by large-scale flow and deformation (Kaminski & Ribe 2002). It is therefore crucial to take anisotropy into account when imaging the mantle. Comparing combined modelling in geodynamics and mineral physics with 3-D maps of seismic anisotropy provides unique information about mantle dynamics and tectonic processes (Becker *et al.* 2006). The first body-wave signature of mantle anisotropy was found in azimuthal variations of *Pn*-wave speeds in oceanic regions (Hess 1964). Teleseismic *P*-wave residuals have also been used to constrain anisotropy (Grésillaud & Cara 1996; Plomerová *et al.* 1996). However, recently, the most popular method to map anisotropy from body-wave observations has been to exploit shear-wave splitting. Being radially polarized in isotropic earth models, *SKS* waves are especially well suited to this approach, and several techniques have been proposed to measure *SKS* splitting (Silver & Chan 1988; Vinnik *et al.* 1989; Savage 1999; Chevrot 2000).

Body-wave studies of anisotropy are usually based on an asymptotic description of wave propagation (i.e. ray theory). Asymptotic body-wave propagation in weakly anisotropic models is well developed (Jech & Pšenčík 1989; Farra 2001; Chen & Tromp 2007). There is firm belief that significant progress in imaging Earth structure requires consideration of the finite-frequency aspects of wave propagation. This has motivated the development of numerical and analytical methods to calculate finite-frequency Fréchet derivatives, or sensitivity kernels, representing changes in seismic observables due to changes in structure (Marquering *et al.* 1999; Dahlen *et al.* 2000; Zhao *et al.* 2005; Zhao & Jordan 2006). Thus far, the application of these methods to compute sensitivity kernels has been limited to isotropic structures, and it is not well understood how finite-frequency seismic observables ‘sense’ anisotropy. For example, the precise region sampled by *SKS*-splitting measurements is still uncertain. *SKS* splitting is usually assumed to provide excellent lateral resolution but limited vertical resolution. Much of the interpretation consists of determining where the anisotropy should be located in depth (Alsina & Snieder 1995; Silver 1996; Savage 1999).

Recently, Favier & Chevrot (2003) have provided some answers to this question. They applied Born-scattering theory, using a plane-wave formalism, to analytically describe the sensitivity kernels of Chevrot's (2000) 'splitting intensity' for SKS waves.

An alternative, but more general, approach to calculating the sensitivity of seismic waves to any structural parameter involves the combination of adjoint methods with spectral-element modelling of seismic wave propagation (Tromp *et al.* 2005; Liu & Tromp 2006, 2007). This approach has proven to be a powerful tool to numerically compute sensitivity kernels in any 3-D earth model. In a previous paper (Sieminski *et al.* 2007), we used this tool to investigate the sensitivity to anisotropy of fundamental-mode surface waves. We continue this work for body waves in this paper.

We explain in Section 2 how we parametrize anisotropy and briefly review the adjoint spectral-element method for the computation of anisotropic sensitivity kernels. In Section 3, we define the  $P$ - and  $S$ -wave traveltimes before discussing their sensitivity kernels for direct waves at teleseismic distances. The specific example of SKS splitting is addressed in Section 4, before concluding.

## 2 ANISOTROPY AND ADJOINT SPECTRAL-ELEMENT SENSITIVITY KERNELS

### 2.1 Parametrization of anisotropy

The elastic structure of the mantle is described by a fourth-order elastic tensor relating the strain to the stress, whose components are denoted  $c_{ijkl}$ ,  $i, j, k, l = 1, 2, 3$ . Due to symmetry properties, the elastic tensor has only 21 independent components (e.g. Babuška & Cara 1991). To assess the effects of anisotropy, we must thus analyse the sensitivity to 21 model parameters. These 21 independent components of the elastic tensor may be rewritten using Voigt's notation with contracted indices as  $C_{IJ}$ ,  $I, J = 1, \dots, 6$  (e.g. Babuška & Cara 1991). The definition of the parameters  $C_{IJ}$  in terms of the corresponding elements  $c_{ijkl}$  of the elastic tensor in spherical coordinates is given in Appendix A. Specific combinations of these  $C_{IJ}$  appear naturally when considering asymptotic wave propagation. In this approximation, an anisotropic perturbation in surface-wave phase speed is determined by an even Fourier series in  $\xi$ , the local azimuth. As first demonstrated by Smith & Dahlen (1973), this series involves degrees zero, two and four. Montagner & Nataf (1986) and Larson *et al.* (1998) expressed the coefficients of the series in terms of a linear combination of perturbations of the  $C_{IJ}$  for plane and spherical layercake models, respectively. The five parameters associated with degree zero are the perturbations of the Love parameters  $\{A, C, N, L, F\}$  (Love 1911) corresponding to transverse isotropy (Appendix B). The azimuthal variation of surface waves is controlled by the parameters  $\{B_{c,s}, H_{c,s}, G_{c,s}\}$  for the 2- $\xi$  variations and  $\{E_{c,s}\}$  for the 4- $\xi$  variations, where the subscripts 'c' and 's' refer to a  $\cos n\xi$  or  $\sin n\xi$ ,  $n = 2, 4$ , dependence, respectively. Anisotropic surface-wave tomography usually describes the model in terms of the Love parameters and the eight azimuthal parameters. Jech & Pšenčík (1989) demonstrated that asymptotic body-wave propagation in weakly anisotropic media is similarly governed by a Fourier series in  $\xi$  involving degrees zero, two and four, but also degrees one and three. Chen & Tromp (2007) expanded on Jech & Pšenčík's (1989) formulation. In addition to the previous 13 parameters for the 0- $\xi$ , 2- $\xi$  and 4- $\xi$  dependence, they introduced eight new elastic parameters  $\{J_{c,s}, K_{c,s}, M_{c,s}\}$  and  $\{D_{c,s}\}$  corresponding to linear combinations of  $C_{IJ}$  describing the 1- $\xi$  and 3- $\xi$  variations, respectively. The five transversely isotropic parameters, the eight azimuthal surface-wave parameters, and the additional eight azimuthal body-wave parameters define a complete parametrization of a general anisotropic medium. In the following, we will refer to these parameters as the 'Chen & Tromp' parameters. The relationship between the Chen & Tromp parameters and the  $C_{IJ}$  is given in Appendix A. Tromp *et al.* (2005) and Liu & Tromp (2006) showed that seismic traveltimes are more efficiently described by wave speeds rather than elastic parameters and density. In this study, we are interested in traveltimes observables, and, therefore, we chose to analyse the sensitivity to the squared wave speeds associated with the Chen & Tromp parameters. These 21 anisotropic squared wave speeds are simply the density-normalized elastic parameters. We denote them with a prime, for example  $A' = A/\rho$ . When studying anisotropy, seismologists often assume transverse isotropy. Only five elastic parameters are needed in this case. A transversely isotropic structure with a vertical symmetry axis may be described by the speeds  $\alpha_h, \alpha_v, \beta_h, \beta_v$  and the dimensionless parameter  $\eta$  (Section B1 of Appendix B). The Preliminary Reference Earth Model (PREM, Dziewonski & Anderson 1981) is a widely used example of a transversely isotropic earth model with a vertical symmetry axis. The sensitivity to these transversely isotropic parameters will be discussed as well.

### 2.2 Adjoint spectral-element method

Adjoint methods were introduced in seismic imaging by Tarantola (1984) for acoustic waves and by Tarantola (1987, 1988) for elastic waves. Recently, Tromp *et al.* (2005) drew connections between this method and finite-frequency ('banana-doughnut') sensitivity kernels (Marquering *et al.* 1999; Dahlen *et al.* 2000). Based on this work, Tape *et al.* (2007) proposed a strategy for 'adjoint tomography'. We will briefly summarize the basis of Tromp *et al.*'s (2005) approach. Details regarding the mathematical aspects of adjoint methods and sensitivity kernels may also be found in Liu & Tromp (2006, 2007). In this study, we are interested in the kernels that describe, in a Born-scattering formalism, how a first-order perturbation of a model parameter affects a seismic observable. Tromp *et al.* (2005) demonstrated that the sensitivity kernels  $K_{\delta c_{jklm}}$  for a perturbation of the elastic parameters  $\delta c_{jklm}$  at location  $\mathbf{x}$  may be expressed as the interaction between a regular displacement wavefield  $\mathbf{s}$ , propagating from the source to the receiver, and an 'adjoint' wavefield  $\mathbf{s}^\dagger$ , which propagates from the receiver to the source:

$$K_{\delta c_{jklm}}(\mathbf{x}) = - \int_0^T e_{jk}^\dagger(\mathbf{x}, T-t) e_{lm}(\mathbf{x}, t) dt, \quad (1)$$

where  $t$  denotes time,  $[0, T]$  the time interval of interest, and  $e_{jk}^\dagger$  and  $e_{lm}$  the components of the strain tensors associated with the adjoint wavefield  $\mathbf{s}^\dagger$  and regular wavefield  $\mathbf{s}$ , respectively. The definition of the adjoint wavefield is intimately linked to the type of observable under consideration. Most seismic observables are constructed from the difference between observed and synthetic waveforms. They are expressed in terms of perturbations in displacement as

$$o_i = \int_0^T \psi_i(\mathbf{x}_r, t) \delta s_i(\mathbf{x}_r, t) dt \quad (\text{no summation over } i), \quad (2)$$

where  $o_i$  denotes the observable,  $\delta s_i$  the  $i$ th component of the perturbed displacement field,  $\mathbf{x}_r$  the receiver position and  $\psi_i$  a function determined by the kind of observable. The adjoint wavefield corresponding to the observable  $o_i$  is generated at the receiver by the adjoint source

$$f_i^\dagger(\mathbf{x}, t) = \psi_i(\mathbf{x}_r, T - t) \delta(\mathbf{x} - \mathbf{x}_r). \quad (3)$$

In this paper, we calculate the wavefields  $\mathbf{s}$  and  $\mathbf{s}^\dagger$  with the spectral-element method developed by Komatitsch & Vilotte (1998) and further extended for global wave propagation in anisotropic models including 3-D crustal & mantle models, ellipticity topography and bathymetry, oceans, the Earth's rotation and self-gravitation (Komatitsch & Tromp 2002a,b; Chen & Tromp 2007). The numerical implementation of the adjoint spectral-element method to calculate sensitivity kernels is detailed by Liu & Tromp (2006) for regional-scale problems and by Liu & Tromp (2007) at the scale of the globe. Other numerical methods can be used to simulate wave propagation and compute kernels. For example, Zhao *et al.* (2005) used a finite-difference method to calculate regional-scale, isotropic sensitivity kernels. Several analytical approaches have been developed to compute finite-frequency isotropic sensitivity kernels. For example, Dahlen *et al.* (2000) used a ray-based method, while Zhao & Jordan (2006) adopted a full-wave approach based upon a normal-mode formalism. With numerical methods, such as spectral-element and finite-difference techniques, we can efficiently compute the sensitivity of any seismic observable, written in the form of eq. (2), for any portion of the seismogram, for the full wavefield. We are not limited to the few seismic arrivals defined by classical ray theory. Normal-mode methods (e.g. Zhao & Jordan 2006) have the same advantage but, contrary to analytical approaches, numerical methods do not require 1-D reference models, they can calculate sensitivity kernels in any 3-D model.

The computation of sensitivity kernels with the adjoint spectral-element method requires one forward simulation to build the adjoint source (eq. 3), and a combined forward and adjoint simulation to construct the kernels according to eq. (1). The results of this approach are kernels that reflect the sensitivity to anisotropic model perturbations  $\delta c_{ijkl}$ . We combine these 'primary' kernels to obtain kernels for the Chen & Tromp parameters (Appendix A). The sensitivity kernels for the squared anisotropic wave speeds are then simply proportional to the elastic kernels, for example,  $K_{\delta A'} = \rho K_{\delta A}$  (Sieminski *et al.* 2007). Kernels for isotropic parameters (such as the isotropic  $P$ -wave speed  $\alpha$  and  $S$ -wave speed  $\beta$ ) may be obtained by combining the anisotropic kernels according to eqs (B5) and (B6). This gives results in agreement with the isotropic kernels of Zhao *et al.* (2005), Hung *et al.* (2000) and Liu & Tromp (2006, 2007), who calculated isotropic kernels directly from the interaction between the regular and adjoint wavefields (eqs 17, 18 and 20 of Tromp *et al.* 2005).

In the next section we apply the adjoint spectral-element method to compute sensitivity kernels for teleseismic  $P$  and  $S$  waves. We will see that  $S$  waves require the introduction of specific observables, and we will define a generalized traveltime anomaly and a generalized 'splitting intensity'. Because the physical interpretation of  $S$ -wave sensitivity is not straightforward, we initially divide the  $S$ -wave analysis into pure  $SV$ - and  $SH$ -wave cases. These experiments allow us to describe the general sensitivity of body waves to anisotropy.

### 3 P- AND S-WAVE SENSITIVITY

#### 3.1 P wave

##### 3.1.1 P-wave observable and adjoint source definition

The common observable for isotropic imaging is the traveltime anomaly  $\delta T$  of the selected wave relative to its theoretical arrival time in the reference model. It is often measured by cross-correlation between the observed signal  $\mathbf{d}$  and the synthetic signal  $\mathbf{s}$  calculated in the reference model. This technique assumes a small perturbation, that is, the traveltime anomaly is assumed to be small compared to the period of the signal and the waveform of the observed pulse is similar to the synthetic one. The approach can be applied to study anisotropic quasi- $P$  waves based upon an isotropic reference model, because  $P$  waveforms are only slightly affected by weak anisotropy (Chen & Tromp 2007). Using the notation of Jech & Pšeničák (1989) and Chen & Tromp (2007), we write the reference isotropic  $P$ -wave signal as

$$\mathbf{s}(\mathbf{x}, t) = s_3(\mathbf{x}, t) \hat{\mathbf{e}}_3, \quad (4)$$

where  $\hat{\mathbf{e}}_3$  denotes the unit vector corresponding to the  $P$ -wave polarization. The quasi- $P$ -wave polarization is usually very close to the isotropic  $P$ -wave polarization (e.g. Farra 2001). The anisotropic quasi- $P$  wave recorded at the receiver  $\mathbf{x}_r$  is thus to first order

$$\mathbf{d}(\mathbf{x}_r, t) = s_3(\mathbf{x}_r, t - \delta T_3) \hat{\mathbf{e}}_3 \simeq [s_3(\mathbf{x}_r, t) - \delta T_3 \dot{s}_3(\mathbf{x}_r, t)] \hat{\mathbf{e}}_3 = [s_3(\mathbf{x}_r, t) + \delta s_3(\mathbf{x}_r, t)] \hat{\mathbf{e}}_3, \quad (5)$$

where we have defined

$$\delta s_3 = -\delta T_3 \dot{s}_3, \quad (6)$$

and where  $\delta T_3$  denotes the  $P$ -wave traveltime anomaly and  $\dot{s}_3$  the time derivative of the displacement. We use the convention of a positive traveltime anomaly  $\delta T$  for a delay of the observed pulse relative to the synthetic one. The cross-correlation between the synthetic and observed  $P$ -wave signals,

$$\Gamma_3(\tau) = \int s_3(\mathbf{x}_r, t - \tau) \dot{s}_3(\mathbf{x}_r, t) dt, \quad (7)$$

reaches its maximum for  $\tau \simeq \delta T_3$ , where (Marquering *et al.* 1999; Dahlen *et al.* 2000; Tromp *et al.* 2005)

$$\delta T_3 = -\frac{1}{N_3} \int \dot{s}_3(\mathbf{x}_r, t) \delta s_3(\mathbf{x}_r, t) dt. \quad (8)$$

The normalization factor  $N_3$  is defined by  $N_3 = \int \dot{s}_3^2 dt$ , and the time integral is over the  $P$ -wave time window. According to eqs (2) and (3), the adjoint source function associated with  $\delta T_3$  is (Tromp *et al.* 2005)

$$\mathbf{f}_3^\dagger(\mathbf{x}, t) = -\frac{1}{N_3} \dot{s}_3(\mathbf{x}_r, T - t) \delta(\mathbf{x} - \mathbf{x}_r) \hat{\mathbf{e}}_3. \quad (9)$$

### 3.1.2 $P$ -wave adjoint kernels

We analyse  $P$ -wave adjoint sensitivity kernels for the squared wave speeds derived from the Chen & Tromp parameters. Throughout this study, the synthetic seismograms from which the adjoint sources are built are computed by spectral-element simulation (Section 2) in spherically symmetric, isotropic PREM (Dziewonski & Anderson 1981). For the  $P$ -wave analysis, the source is a vertical point force located at the South Pole at 600 km depth, the source–time function is a Gaussian with a half duration of 11 s, and the epicentral distance is  $75^\circ$ . To compute the adjoint source function we low-pass filter the seismograms with a corner at 14.5 s to limit the high-frequency signal in the adjoint wavefield. The time window used to isolate the wave of interest is a Welch taper defined as  $w(t) = 1 - (2t/\Delta t - 1)^2$ , with  $\Delta t$  the width of the time-window (Press *et al.* 1992). The  $P$ -wave traveltime anomaly  $\delta T_3$  is usually measured from vertical-component recordings. We follow this simplification here and consider a purely vertical adjoint source function  $\mathbf{f}_3^\dagger$ . The adjoint source–time function and the selected vertical synthetic signal are shown in Fig. 1. We obtain very similar results if we use the signal on the  $P$ -wave polarization direction rather than the vertical component. Only the kernels for the azimuthally anisotropic ‘ $c$ -parameters’ ( $J'_c, K'_c, M'_c, B'_c, H'_c, G'_c, D'_c$  and  $E'_c$ ) are shown in Fig. 2, because the kernels for the ‘ $s$ -parameters’ ( $J'_s, K'_s, M'_s, B'_s, H'_s, G'_s, D'_s$  and  $E'_s$ ) have the same characteristics. To avoid clutter, we will drop the subscripts  $c$  and  $s$  in the following, unless needed. The kernels are displayed in a vertical section throughout the mantle in the source–receiver great-circle plane. In this plane, the kernels for isotropic model perturbations are ‘banana’ shaped (Fig. 3), while a vertical section orthogonal to this plane would picture a ‘doughnut’ shape in a 1-D reference model (Marquering *et al.* 1999; Hung *et al.* 2000).

We still recognize the banana–doughnut pattern in the anisotropic kernels.  $P$  waves are sensitive to a finite volume around the geometrical ray (Figs 2 and 3). The maximum sensitivity is off the ray path, while the sensitivity is zero along the ray path, like in Liu & Tromp (2007), Zhao & Jordan (2006), Hung *et al.* (2000) and Marquering *et al.* (1999), except in the vicinity of the source and the receiver because of near-field effects, as discussed by Favier *et al.* (2004). The high sensitivity close to the source and the receiver is partly due to a geometrical focusing effect (Marquering *et al.* 1999; Dahlen *et al.* 2000). Anisotropy strongly affects this general pattern. We see large variations of the kernel amplitude along the ray path (Fig. 2) that cannot be explained by the source radiation. The sensitivity is minimal at the turning point for  $C', L', F', H'$  and  $G'$ . In addition to cancelling at the turning point, the sensitivity exhibits a sign change for the body-wave parameters  $J', K'$  and  $D'$ . The same  $J'$ -anomaly thus causes opposite traveltime anomalies depending on whether the wave is going up or down. Except in the vicinity of the source and the receiver,  $P$  waves are virtually insensitive to  $N'$  and  $M'$ .

Adjoint kernels are Born kernels (eq. 1), and thus are fully consistent with Born-scattering theory (Zhou *et al.* 2006; Sieminski *et al.* 2007). In a Born-scattering formalism, the sensitivity patterns are partly due to variations in the scattering coefficients with the 3-D polarizations and propagation directions of the incident and scattered wavefields (Dahlen *et al.* 2000). Contrary to the isotropic case, the radiation pattern of the scattering coefficients for an anisotropic perturbation varies with the orientation of the incident wave (Calvet *et al.* 2006). Asymptotically, this

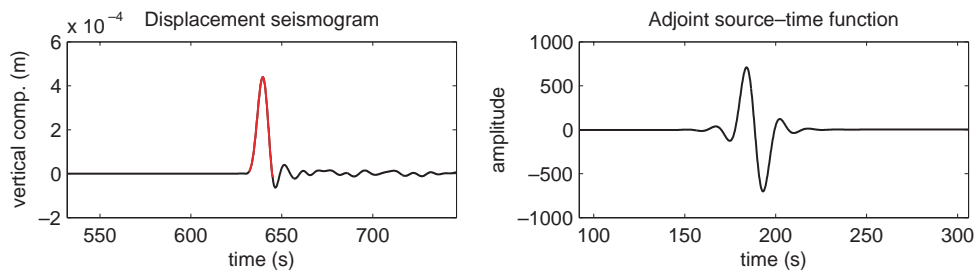


**Figure 1.** Synthetic displacement seismogram calculated for the vertical component (left-hand panel) of a receiver at  $75^\circ$  from a vertical point force source (black line). The red portion corresponds to the  $P$ -wave time window selected to build the adjoint source–time function (right-hand panel) (eq. 9). The signal is low-pass filtered with a corner at 14.5 s before calculating the adjoint source–time function, and the time window to select the  $P$ -wave arrival is a Welch taper. The adjoint source–time function is used to compute the kernels displayed in Figs 2 and 3.

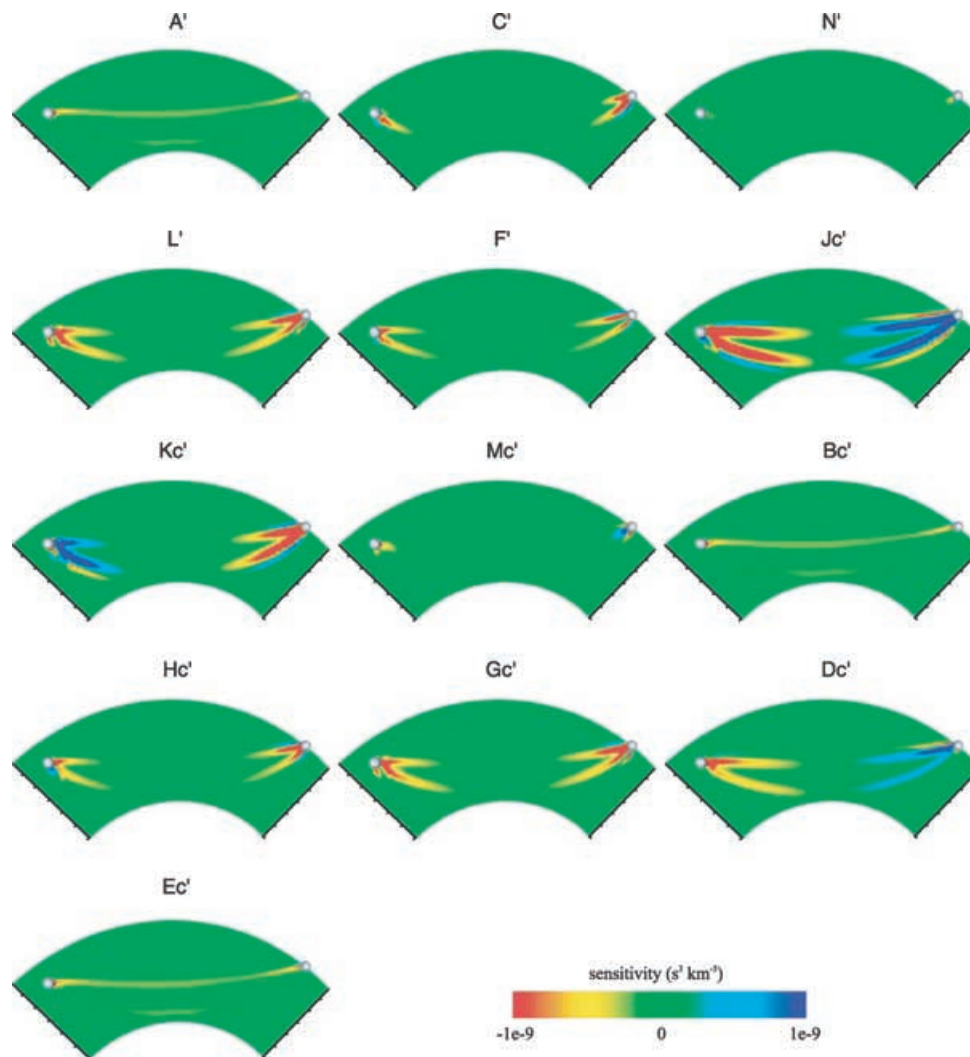


**Figure 2.** Adjoint sensitivity kernels of the observable  $\delta T_3$ , the  $P$ -wave cross-correlation traveltime anomaly (eq. 8), at a dominant period of 15 s, for 13 of the anisotropic squared wave speeds derived from the Chen & Tromp parameters. The epicentral distance is  $75^\circ$  and the source is a vertical point force located at the South Pole at 600 km depth. The source (left-hand side) and receiver (right-hand side) are represented by a small grey sphere. The kernels are displayed on a depth-section throughout the mantle along the source–receiver great-circle plane. The tick marks of the depth scale are situated every 500 km from the core–mantle boundary to the surface.

complicated scattering effect reduces to a dependence of the sensitivity on the local orientation of the geometrical ray given by the incidence angle  $i$  and the azimuth  $\xi$  along the path. This directional dependence has been analysed by Chen & Tromp (2007). Their formulation is sufficient to understand the specific amplitude variations of the adjoint kernels. The significant sensitivity is indeed limited to the first Fresnel zone, where the orientation of the incident and scattered waves is very close to the orientation of the geometrical ray. Fig. 4 shows Chen & Tromp's (2007) prediction of the variations as a function of  $i$  and  $\xi$  of the  $P$ -wave traveltime anomaly for perturbations of the elastic parameters  $A'$  and  $J'$ . These predictions are in good agreement with the amplitude variations of the adjoint kernels shown in Fig. 2. Because the local azimuth is constant and equal to  $180^\circ$  for this specific path, Fig. 2 emphasizes the effects of the incidence angle. We can identify 'horizontal' propagation parameters ( $A'$ ,  $B'$  and  $E'$ ), to which  $P$  waves are sensitive when the path has a significant horizontal component, that is, around the turning point (where  $i \simeq 90^\circ$ ). We recognize  $C'$  as the 'vertical' propagation parameter. The other parameters are only involved for propagation at intermediate incidence angles. For example, the  $P$ -wave traveltime anomaly is sensitive to a perturbation of the  $S$ -wave parameter  $L'$  at intermediate incidence angles. Since in general the incidence angle and the azimuth vary along the ray path, Fig. 4 predicts complicated sensitivity patterns. For a constant local azimuth, only the body-wave parameters exhibit sign changes in sensitivity (Fig. 2). For paths with strong azimuthal variations, sign changes may be expected for some surface-wave parameters as well. The sensitivity to the transversely isotropic parameters does not present sign changes, at least not in an isotropic 1-D reference model. In general, the influence of  $i$  and  $\xi$  makes the sensitivity highly path-dependent, as we will see for  $SKS$  waves in Section 4 (Fig. 18).

We note that the sensitivity to the azimuthally anisotropic parameters  $J'$  and  $K'$  may be much higher than for the transversely isotropic parameters (Fig. 2), from which the isotropic speeds are derived (Section B1 of Appendix B). The sensitivity to  $J'$  is about one order of magnitude higher than the sensitivity to  $A'$  or  $C'$  in Fig. 2. This confirms Chen & Tromp's (2007) identification of  $J'$  and  $K'$  as the prominent

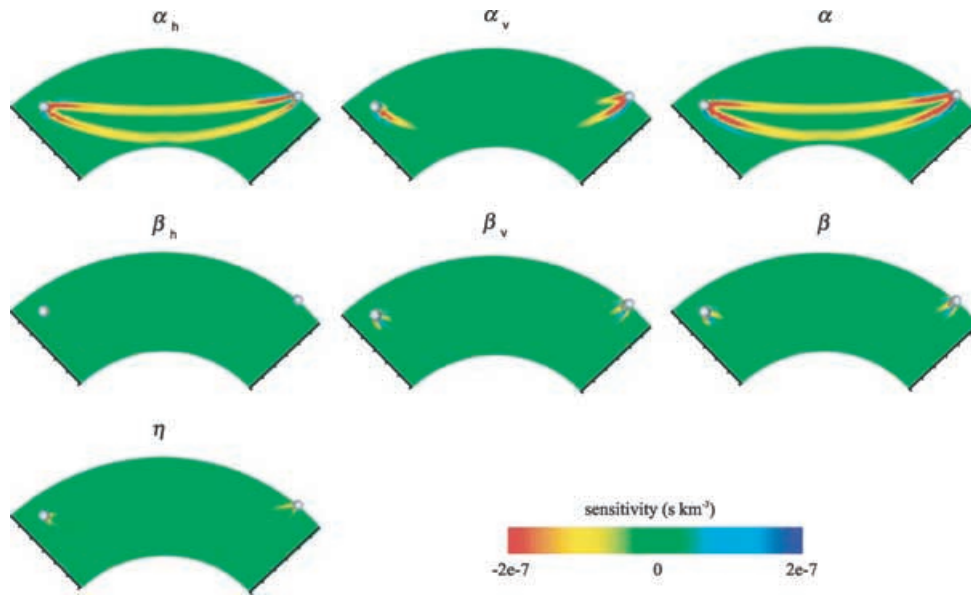


**Figure 3.** Same as Fig. 2 but for relative perturbations of the four transversely isotropic wave speeds  $\delta\alpha_h/\alpha_h$ ,  $\delta\alpha_v/\alpha_v$ ,  $\delta\beta_h/\beta_h$  and  $\delta\beta_v/\beta_v$  and the dimensionless parameter  $\delta\eta/\eta$  (left-hand and middle columns), and for the two isotropic speeds  $\delta\alpha/\alpha$  and  $\delta\beta/\beta$  (right-hand column). The relations between the Chen & Tromp kernels and these kernels are given in Section B1.

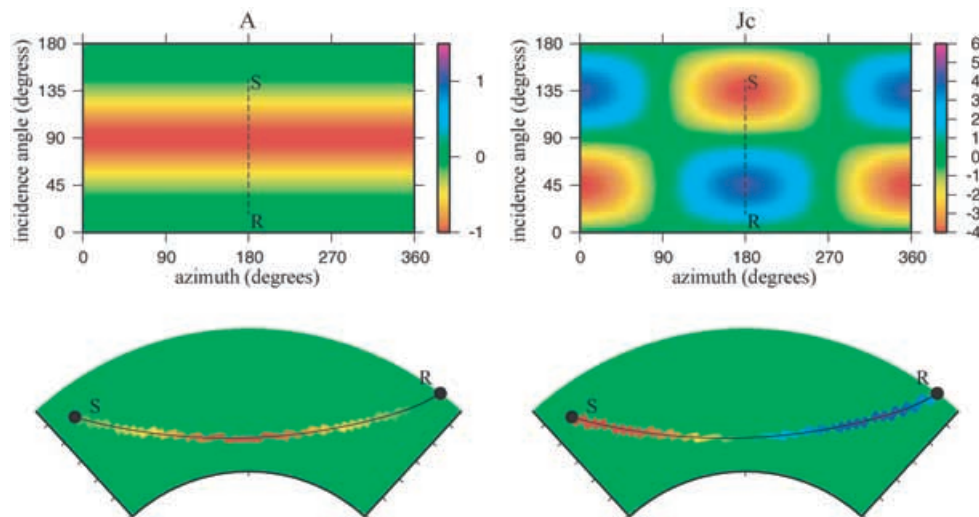


**Figure 4.** Asymptotic directional dependence of the  $P$ -wave travelt ime anomaly  $\delta T_3$  as a function of ray azimuth  $\xi$  and incidence angle  $i$  for the parameters  $A$  (top left-hand side) and  $J_c$  (top right-hand side) from Chen & Tromp's (2007) analysis. Colours indicate percentage of travelt ime anomaly for a 1 per cent-perturbation of the elastic parameters. The asymptotic directional dependence of the  $P$ -wave travelt ime anomaly for the other azimuthally anisotropic parameters is displayed in Fig. 17 of Chen & Tromp (2007). Asymptotic directional dependence of the  $P$ -wave travelt ime anomaly along the geometrical ray corresponding to the experiment shown in Fig. 2 for the parameters  $A$  (bottom left-hand side) and  $J_c$  (bottom right-hand side). The location of the ray in the  $(\xi, i)$  coordinates is indicated in the top figures by a dashed line. The colour scale is the same for the top and bottom figures for the same parameter.

parameters for  $P$  waves. The high  $P$ -wave sensitivity to  $J'$  and  $K'$  also explains the large  $1-\xi$  component of the azimuthal variations of  $P$ -wave travelt ime anomalies computed in anisotropic models (Schulte-Pelkum & Balckman 2003), as well as the predominant 'bipolarity' of observed  $P$ -wave residuals with azimuth (Plomerová *et al.* 1996). The non-sensitivity of  $P$  waves to  $N'$  and  $M'$  is in good agreement with previous interpretations of these parameters. The parameter  $N'$  controls horizontally propagating SH waves, and the parameters  $M'$  are involved in the rotation of the  $S$ -wave polarization plane (Chen & Tromp 2007).

In Fig. 3, we consider a transversely isotropic structure with a vertical symmetry axis. Only five elastic parameters are now needed, and we choose a parametrization in terms of wave speeds (Section B1). As expected,  $P$  waves are mainly sensitive to  $\alpha_h$ , because the orientation of the path considered here has a large horizontal component, and to  $\alpha_v$  close to the source and the receiver when the propagation direction is more vertical. In disagreement with asymptotic predictions,  $P$  waves are somewhat sensitive to  $\beta_v$  in the vicinity of the source and the receiver, and consequently to perturbation of the isotropic shear-wave speed  $\beta$ , the  $\beta$ -kernel being the sum of the kernels for  $\beta_v$  and  $\beta_h$  (eq. B6). This can be explained by a combination of non-forward scattered  $P$  and  $SV$  waves and geometrical focusing. Perturbations of the

isotropic shear-wave speed  $\beta$  do not cause forward scattering for  $P$  waves but they do produce  $P$ -to- $P$ ,  $SV$ -to- $P$  and  $P$ -to- $SV$  scattering in the plane of the ray path (Dahlen *et al.* 2000). These scattered waves are weak compared to the scattering effect of perturbations of the isotropic  $P$ -wave speed  $\alpha$ . However, because of geometrical focusing, they can significantly influence the sensitivity in the vicinity of the source and the receiver. Apart from this,  $P$ -wave sensitivity is well explained by  $P$ -to- $P$  near-forward scattering.

A dominant period of 15 s is relatively long for body-wave data. Analysis of the dependence of the sensitivity on wave period shows that the width of the finite-frequency kernels scales linearly with the square root of the wavelength (e.g. Hung *et al.* 2000). When the period decreases, the kernels will accordingly become narrower, while their overall amplitude will increase, as shown in, for example, Liu & Tromp (2007), Favier & Chevrot (2003) and Marquering *et al.* (1999). At shorter periods, the anisotropic kernels will however retain the characteristics discussed above, because the directional dependence does not depend on the period (Dahlen *et al.* 2000; Calvet *et al.* 2006).

## 3.2 S waves

### 3.2.1 S-wave observables and adjoint source definition

Unlike  $P$  waveforms,  $S$  waveforms are strongly affected by anisotropy (Fig. 5). In (weakly) anisotropic structures,  $S$  waves are split into two quasi- $S$  waves orthogonally polarized and propagating with different speeds. We label the fast and slow quasi- $S$  waves  $S_1$  and  $S_2$ , respectively. The unit vectors corresponding to their respective polarization directions are denoted  $\hat{\mathbf{g}}_1$  and  $\hat{\mathbf{g}}_2$  (Fig. 6). Thus, typically two arrivals are recorded at the receiver in the  $S$ -wave time window on both the  $SV$  and  $SH$  components. We cannot write the  $SV$ - and  $SH$ -component arrivals in the form of eq. (5). The traditional cross-correlation measure of traveltime anomalies is, therefore, not appropriate, and other observables are needed to analyse  $S$  waves in anisotropic media. The usual  $S$ -wave splitting measurements are the split traveltime anomaly  $\Delta T$  between the two quasi- $S$  waves, and the azimuth of the apparent polarization of the fast wave. To simplify the notations in the following, we introduce the angle  $\phi$  between the apparent polarization of the fast wave and the radial direction (Fig. 6). If observed on the fast and slow polarization directions  $\hat{\mathbf{g}}_1$  and  $\hat{\mathbf{g}}_2$ , the two quasi- $S$  waves separate and we can measure their traveltime anomalies relative to the reference isotropic  $S$  wave,  $\delta T_1$  and  $\delta T_2$ , respectively. Then  $\Delta T = \delta T_2 - \delta T_1$ , and we introduce  $\delta \bar{T} = \frac{1}{2}(\delta T_1 + \delta T_2)$  to denote the average of the two anomalies. The average traveltime anomaly is generally non-zero, that is, the arrival times of  $S_1$  and  $S_2$  are not symmetric relative to the reference time

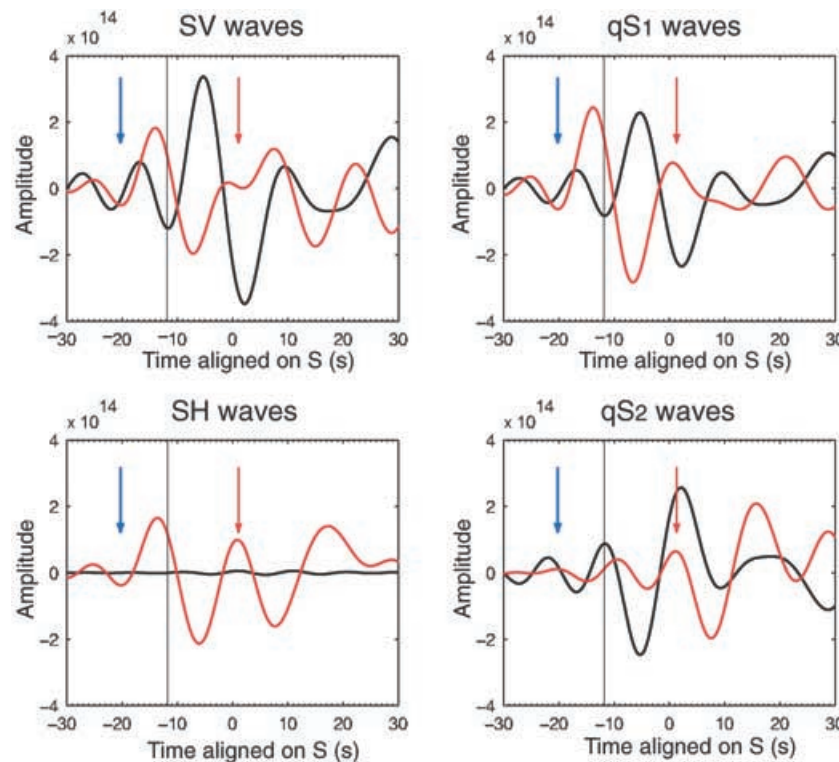


**Figure 5.** Shear waveforms from spectral-element simulations in isotropic PREM (black lines) and an anisotropic model (red lines) calculated at an epicentral distance of  $75^\circ$  from a vertical point force source generating  $P$  and  $SV$  waves only. Vertical lines correspond to the reference  $S$ -wave arrival time in isotropic PREM. Blue arrows indicate the predicted arrival time of quasi- $S$  wave  $S_1$  and red arrows the predicted arrival time of quasi- $S$  wave  $S_2$ . In the left-hand column, the waveforms are observed on the  $SV$  and  $SH$  polarizations directions. In the right-hand column, they are projected to the  $S_1$  (fast) polarization direction and the  $S_2$  (slow) polarization directions. We especially note that the waveforms are strongly affected by anisotropy and the arrival times of the two quasi- $S$  waves are not symmetric relative to the reference time. Reprinted with permission from Chen & Tromp (2007).

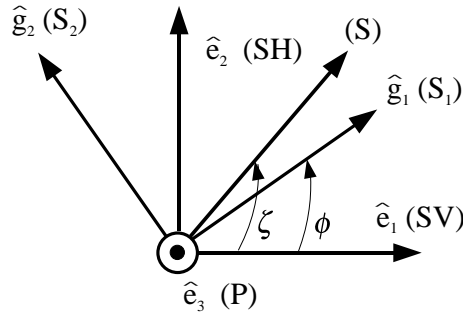


**Figure 6.** Schematic illustration of the polarizations of the reference isotropic shear wave  $S$ , the fast quasi-shear wave  $S_1(\hat{\mathbf{g}}_1)$  and slow quasi-shear wave  $S_2(\hat{\mathbf{g}}_2)$  relative to the  $SV$ -wave,  $SH$ -wave and  $P$ -wave polarization directions ( $\hat{\mathbf{e}}_1, \hat{\mathbf{e}}_2, \hat{\mathbf{e}}_3$ ). We assume that the anisotropic perturbation transfers insignificant  $S$ -wave energy to the  $P$ -wave polarization direction. The polarization angles  $\zeta$  and  $\phi$  are measured counter-clockwise from the  $SV$ -wave polarization direction in a right-handed coordinate system.

(Fig. 5). For weakly anisotropic perturbations,  $\Delta T$  and  $\delta\bar{T}$  are assumed to be small relative to the period of the signal. We express the reference isotropic  $S$ -wave signal as

$$\mathbf{s}(\mathbf{x}, t) = s_1(\mathbf{x}, t) \hat{\mathbf{e}}_1 + s_2(\mathbf{x}, t) \hat{\mathbf{e}}_2, \quad (10)$$

where the unit vectors  $\hat{\mathbf{e}}_1$  and  $\hat{\mathbf{e}}_2$  define the  $SV$ - and  $SH$ -wave polarization directions (Fig. 6). For weak anisotropy, insignificant  $S$ -wave energy is transferred to  $\hat{\mathbf{e}}_3$ , the isotropic  $P$ -wave polarization direction. This is consistent with assuming that the quasi- $P$  wave polarization is very close to its isotropic counterpart (Section 3.1). We will consider a single anisotropic perturbation, similar to Born (single) scattering. With multiple anisotropic perturbations there would be multiple  $S$ -wave splitting. For a single weakly anisotropic perturbation, the  $S$ -wave signal may be written in the form

$$\mathbf{d}(\mathbf{x}, t) = s_{g_1}(\mathbf{x}, t - \delta T_1) \hat{\mathbf{g}}_1 + s_{g_2}(\mathbf{x}, t - \delta T_2) \hat{\mathbf{g}}_2, \quad (11)$$

where  $s_{g_1}$  and  $s_{g_2}$  denote the signals observed along the  $\hat{\mathbf{g}}_1$  and  $\hat{\mathbf{g}}_2$  polarization directions:

$$s_{g_1} = s_1 \cos \phi + s_2 \sin \phi, \quad (12)$$

$$s_{g_2} = -s_1 \sin \phi + s_2 \cos \phi. \quad (13)$$

Inserting eqs (12) and (13) in eq. (11) yields to first order

$$\begin{aligned} \mathbf{d}(\mathbf{x}, t) &\simeq [s_1(\mathbf{x}, t) - \delta\bar{T} \dot{s}_1(\mathbf{x}, t) + \frac{1}{2} \Delta T \cos 2\phi \dot{s}_1(\mathbf{x}, t) + \frac{1}{2} \Delta T \sin 2\phi \dot{s}_2(\mathbf{x}, t)] \hat{\mathbf{e}}_1 \\ &\quad + [s_2(\mathbf{x}, t) - \delta\bar{T} \dot{s}_2(\mathbf{x}, t) - \frac{1}{2} \Delta T \cos 2\phi \dot{s}_2(\mathbf{x}, t) + \frac{1}{2} \Delta T \sin 2\phi \dot{s}_1(\mathbf{x}, t)] \hat{\mathbf{e}}_2 \\ &= [s_1(\mathbf{x}, t) + \delta s_1(\mathbf{x}, t)] \hat{\mathbf{e}}_1 + [s_2(\mathbf{x}, t) + \delta s_2(\mathbf{x}, t)] \hat{\mathbf{e}}_2, \end{aligned} \quad (14)$$

where

$$\delta s_1 = -\delta\bar{T} \dot{s}_1 + \frac{1}{2} \Delta T \cos 2\phi \dot{s}_1 + \frac{1}{2} \Delta T \sin 2\phi \dot{s}_2, \quad (15)$$

$$\delta s_2 = -\delta\bar{T} \dot{s}_2 - \frac{1}{2} \Delta T \cos 2\phi \dot{s}_2 + \frac{1}{2} \Delta T \sin 2\phi \dot{s}_1. \quad (16)$$

Upon comparing eqs (14) and (5), we identify three potential  $S$ -wave observables:  $\delta\bar{T}$ ,  $\frac{1}{2} \Delta T \cos 2\phi$  and  $\frac{1}{2} \Delta T \sin 2\phi$ . For adjoint simulations, these observables must be expressed as linear functions of the perturbed displacement signal (eq. 2). Unfortunately, we were unable to find such linear relationships. Instead, we propose two new quantities,  $o_1$  and  $o_2$ , defined as linear functions of the perturbed  $SV$  signal  $\delta s_1$  and the perturbed  $SH$  signal  $\delta s_2$ :

$$o_1 = -\frac{1}{N_{12}} \int [\dot{s}_1(\mathbf{x}_r, t) \delta s_1(\mathbf{x}_r, t) - \dot{s}_2(\mathbf{x}_r, t) \delta s_2(\mathbf{x}_r, t)] dt, \quad (17)$$

$$o_2 = -\frac{1}{N_{12}} \int [\dot{s}_2(\mathbf{x}_r, t) \delta s_1(\mathbf{x}_r, t) + \dot{s}_1(\mathbf{x}_r, t) \delta s_2(\mathbf{x}_r, t)] dt, \quad (18)$$

where  $N_{12} = \int (\dot{s}_1^2 + \dot{s}_2^2) dt$  and the time integral is over the  $S$ -wave time window. The quantities  $o_1$  and  $o_2$  are easily related to the splitting measurements  $\Delta T$ ,  $\phi$  and  $\delta\bar{T}$ . From the expressions for  $\delta s_1$  and  $\delta s_2$  defined by eqs (15) and (16), we obtain

$$o_1 = -\frac{1}{2} \Delta T \cos 2\phi + \delta\bar{T} \cos 2\zeta, \quad (19)$$

$$o_2 = -\frac{1}{2} \Delta T \sin 2\phi + \delta\bar{T} \sin 2\zeta, \quad (20)$$

where  $\zeta$  is the angle between the polarization of the isotropic reference  $S$  wave and the radial direction (Fig. 6). In other words, if  $s(t)$  denotes the  $S$  isotropic reference waveform, then  $s_1(t) = s(t) \cos \zeta$  and  $s_2(t) = s(t) \sin \zeta$ . The quantities  $o_1$  and  $o_2$  can be constructed from the splitting measurements and the fast polarization direction. We will see in what follows that  $o_1$  is a generalization of the traveltime anomaly and  $o_2$  of the ‘splitting intensity’ first introduced by Chevrot (2000) for  $SKS$  splitting.

The observables  $o_1$  and  $o_2$  have the additional advantage of being related to the two cross-correlations  $\Gamma_1(\tau)$  and  $\Gamma_2(\tau)$  defined by

$$\Gamma_1(\tau) = \int s_1(\mathbf{x}_r, t - \tau) d_1(\mathbf{x}_r, t) + s_2(\mathbf{x}_r, t + \tau) d_2(\mathbf{x}_r, t) dt, \quad (21)$$

$$\begin{aligned} \Gamma_2(\tau) = & \int s_1(\mathbf{x}_r, t - \tau) [d_2(\mathbf{x}_r, t) - s_2(\mathbf{x}_r, t) + s_1(\mathbf{x}_r, t)] \\ & + s_2(\mathbf{x}_r, t - \tau) [d_1(\mathbf{x}_r, t) - s_1(\mathbf{x}_r, t) + s_2(\mathbf{x}_r, t)] dt. \end{aligned} \quad (22)$$

The cross-correlations  $\Gamma_1(\tau)$  and  $\Gamma_2(\tau)$  reach their maximum for  $\tau \simeq o_1$  and  $\tau \simeq o_2$ , respectively. These equations suggest an alternative technique to measure the observables  $o_1$  and  $o_2$  based upon cross-correlation. They confirm these quantities to be temporal observables, since they are measured by extracting time information contained in the seismograms.

From eqs (17) and (18) we can readily derive the adjoint source functions  $\mathbf{f}_1^\dagger$  and  $\mathbf{f}_2^\dagger$  associated with the observables  $o_1$  and  $o_2$ , respectively:

$$\mathbf{f}_1^\dagger(\mathbf{x}, t) = -\frac{1}{N_{12}} [\dot{s}_1(\mathbf{x}_r, T - t) \hat{\mathbf{e}}_1 - \dot{s}_2(\mathbf{x}_r, T - t) \hat{\mathbf{e}}_2] \delta(\mathbf{x} - \mathbf{x}_r), \quad (23)$$

$$\mathbf{f}_2^\dagger(\mathbf{x}, t) = -\frac{1}{N_{12}} [\dot{s}_2(\mathbf{x}_r, T - t) \hat{\mathbf{e}}_1 + \dot{s}_1(\mathbf{x}_r, T - t) \hat{\mathbf{e}}_2] \delta(\mathbf{x} - \mathbf{x}_r). \quad (24)$$

For pure  $SV$  and  $SH$  waves the integral definitions of  $o_1$  and  $o_2$  and their relationships to the splitting measurements simplify, highlighting the link with the traditional traveltime anomaly and the splitting intensity. Next, we investigate  $S$ -wave sensitivity through these new observables for pure  $SV$  and  $SH$  waves.

### 3.2.2 $SV$ -wave adjoint kernels

For pure  $SV$  waves, the isotropic reference  $S$  wave is only observed on the  $SV$ -wave polarization direction, that is,  $s_2(\mathbf{x}_r, t) = 0$  and  $\zeta = 0^\circ$ . The integral definitions (17) and (18) of the observables  $o_1$  and  $o_2$  simplify to

$$o_1 = -\frac{1}{N_1} \int \dot{s}_1(\mathbf{x}_r, t) \delta s_1(\mathbf{x}_r, t) dt, \quad (25)$$

$$o_2 = -\frac{1}{N_1} \int \dot{s}_1(\mathbf{x}_r, t) \delta s_2(\mathbf{x}_r, t) dt, \quad (26)$$

with  $N_1 = \int \dot{s}_1^2 dt$ . The relationships (19) and (20) between  $o_1$  and  $o_2$  and the splitting measurements become

$$o_1 = -\frac{1}{2} \Delta T \cos 2\phi + \delta \bar{T}, \quad (27)$$

$$o_2 = -\frac{1}{2} \Delta T \sin 2\phi. \quad (28)$$

In this case, we recognize  $o_2$  as the splitting intensity of Chevrot (2000). For vertically transversely isotropic perturbations (i.e.  $\delta A'$ ,  $\delta C'$ ,  $\delta N'$ ,  $\delta L'$  and  $\delta F'$ ) Chen & Tromp's (2007) asymptotic formulation predicts that  $\phi = 0^\circ$ . Thus, only one  $S$ -wave arrival is expected on the  $SV$ -component, which leads to  $o_1 = -\frac{1}{2} \Delta T + \delta \bar{T} = \delta T_1$ , that is, the  $SV$ -wave traveltime anomaly.

We compute adjoint sensitivity kernels for the  $SV$ -wave observables  $o_1$  and  $o_2$  for the same source–receiver configuration and parameters (source mechanism, source–time function, epicentral distance, dominant period of the signal, and reference model) as in the  $P$ -wave experiment. The vertical point source is particularly important here to generate  $S$  waves only polarized in the source–receiver great-circle plane. The  $SH$ -wave polarization corresponds to the transverse component, and we identify the  $SV$ -wave polarization at the receiver with the radial component. Fig. 7 shows the selected radial displacement signal and its corresponding adjoint source–time function. Applied on the radial component, this source–time function generates the adjoint wavefield to compute the kernels for the observable  $o_1$  (eq. 23), but it is applied on the transverse component for the observable  $o_2$  (eq. 24). For these teleseismic waves, similar results will be obtained by using the  $SV$ -wave signal instead of the radial-component signal. The adjoint kernels for the Chen & Tromp squared wave speeds are presented in Fig. 8 for  $o_1$  and Fig. 10 for  $o_2$ . In Fig. 9, we show the sensitivity of  $o_1$  to relative perturbations of the transversely isotropic wave speeds and the dimensionless parameter  $\eta$ . For this very specific case of a constant azimuth equal to  $180^\circ$ ,  $o_1$  is not sensitive to the  $s$ -parameters, while the splitting intensity  $o_2$  is not sensitive to the  $c$ -parameters. In general, the sensitivity kernels for the  $c$ - and  $s$ -parameters have the same characteristics.

The  $SV$ -wave kernels in Figs 8–10 exhibit more structure off the first Fresnel zone than the  $P$ -wave kernels shown in Section 3.1. This is a common feature for late arriving waves, especially when recorded on the radial or vertical components (Zhao & Jordan 2006; Liu & Tromp 2007). We use isotropic PREM as the reference model, which has wave-speed discontinuities and gradients. In such models, many possible reflected, refracted and converted waves ( $P$ -to- $SV$ ,  $SV$ -to- $P$ ) arrive on the radial component in the  $SV$ -wave time window. The adjoint spectral-element method, because it is a full-wave approach, considers all these waves and the adjoint kernels are usually very ‘rich’. For

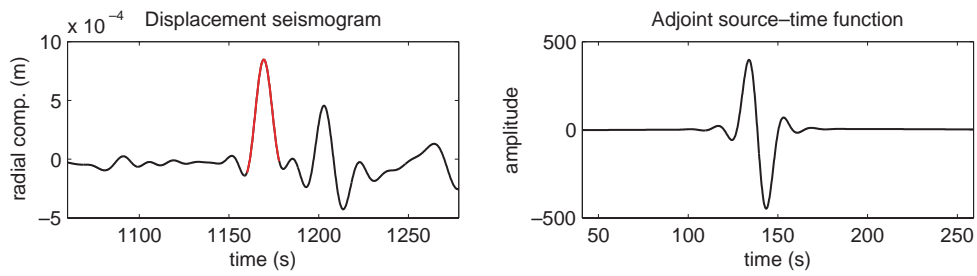


**Figure 7.** Synthetic displacement seismogram calculated for the radial component (left-hand panel) of a receiver at  $75^\circ$  from a vertical point force source (black line). The red portion corresponds to the  $S$ -wave time window selected to build the adjoint source–time function (right-hand panel) associated with the observables  $o_1$  and  $o_2$  (eqs 17 and 18). The signal is low-pass filtered with a corner at 14.5 s before calculating the adjoint source–time function. The adjoint source–time function is applied to the radial component to compute the kernels for  $o_1$  (Figs 8 and 9) and to the transverse component for  $o_2$  (Fig. 10).

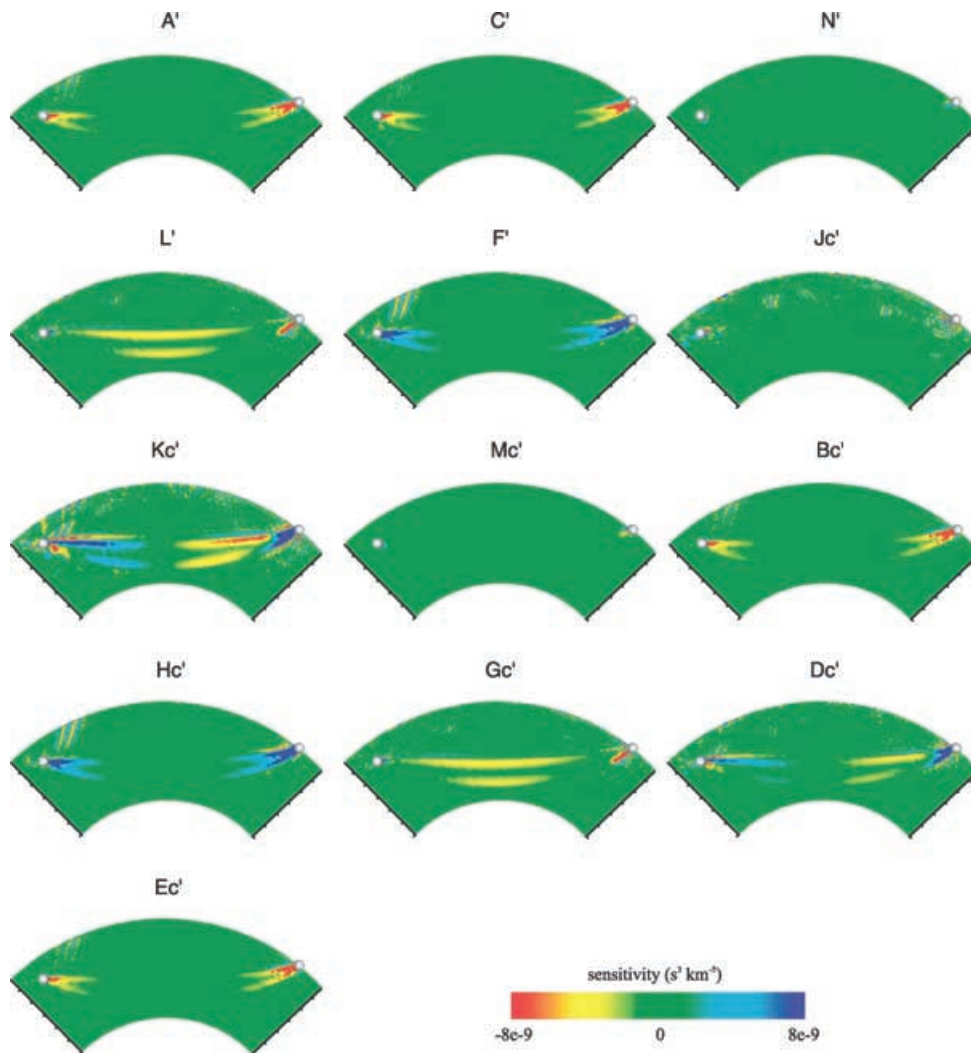


**Figure 8.** Same as in Fig. 2 but for the  $SV$ -wave observable  $o_1$  (eq. 27).

example, the near-vertical sensitivity bands on the source side visible for most of the  $o_1$ -kernels in Figs 8 and 9 can be attributed to  $SV$ -wave energy emitted upward at the source, then travelling to the receiver as guided  $P$ -wave energy in the asthenosphere. Although the  $SV$ -wave kernels are computed at the same period as the  $P$ -wave kernels, their sensitivity zones are narrower (compare Figs 3 and 9). This is because of the smaller wavelength of the  $S$ -waves, since the width of the kernels scales as the square root of the wavelength (e.g. Hung *et al.* 2000). The transversely isotropic and isotropic kernels for  $o_1$  have overall a higher amplitude than the  $P$ -wave kernels. For the same relative perturbation, since  $\alpha > \beta$ ,  $P$ -wave traveltimes are smaller than  $S$ -wave anomalies.

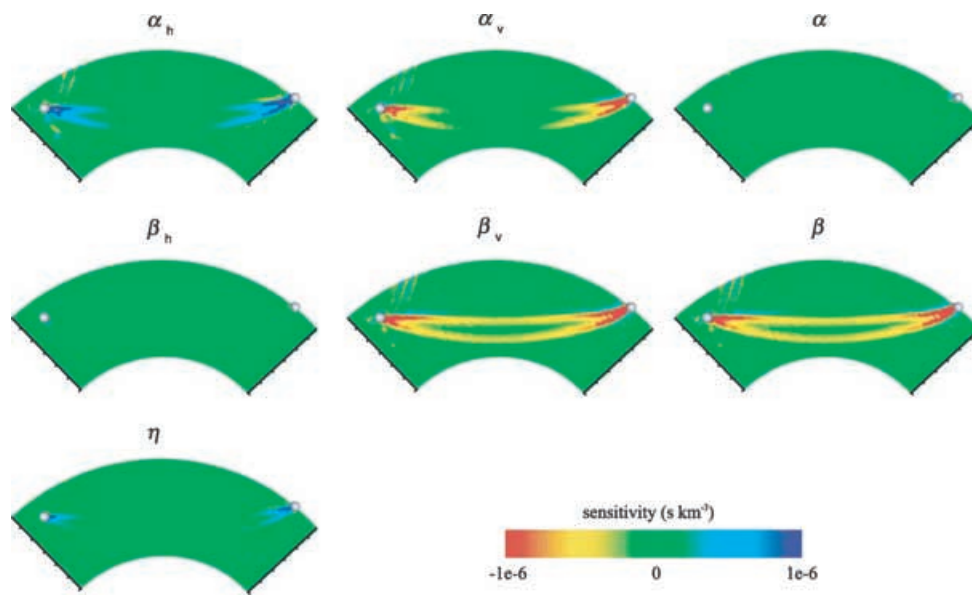


Figure 9. Same as Fig. 3 but for the SV-wave observable  $o_1$  (eq. 27), the SV-wave traveltime anomaly in this case.

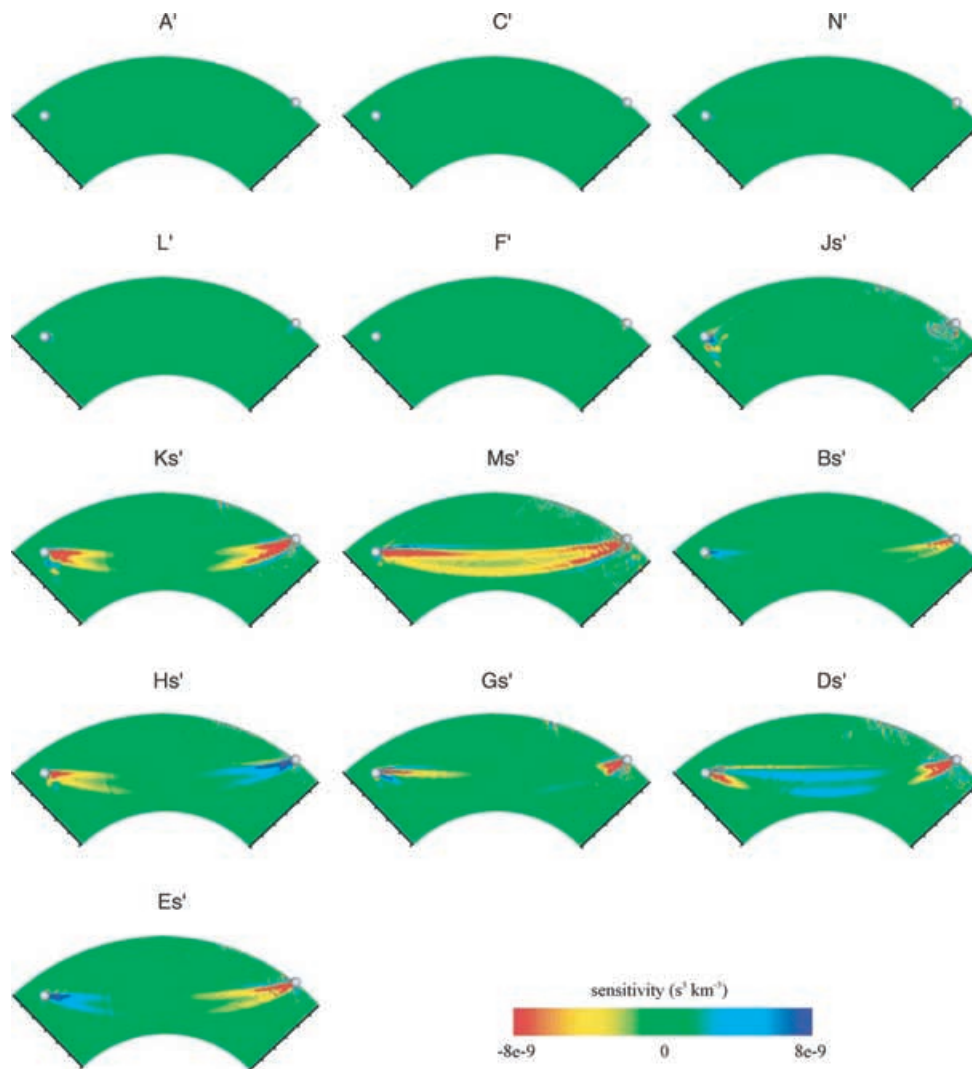
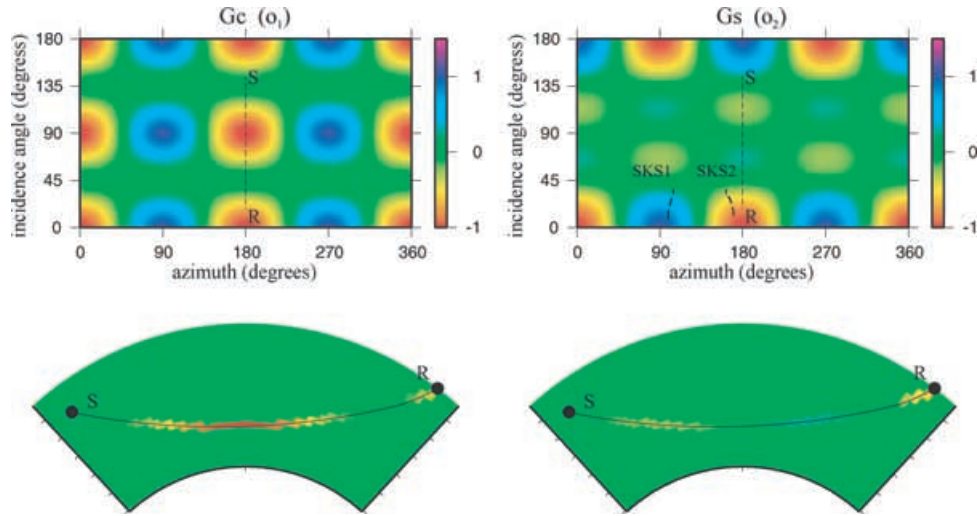


Figure 10. Same as in Fig. 2 but for the SV-wave observable  $o_2$  (eq. 28), the splitting intensity.



**Figure 11.** Asymptotic directional dependence as a function of ray azimuth  $\xi$  and incidence angle  $i$  of the *SV*-wave observables  $o_1$  (generalized traveltime anomaly) for the parameter  $G_c$  (top left-hand panel) and  $o_2$  (splitting intensity) for the parameter  $G_s$  (top right-hand panel) from Chen & Tromp's (2007) analysis. Colours indicate percentage of  $o_1$  and  $o_2$  relative to the *SV*-wave reference traveltime for a 1 per cent-perturbation of the elastic parameters. Asymptotic directional dependence of the *SV*-wave observables  $o_1$  for the parameter  $G_c$  (bottom left-hand side) and  $o_2$  for the parameter  $G_s$  (bottom right-hand side) along the geometrical ray corresponding to the experiments shown in Figs 8 and 10. The location of the ray in the  $(\xi, i)$  coordinates is indicated in the top figures by the S-R dashed line. The dashed lines noted SKS1 ( $\xi_r = 99^\circ$ ) and SKS2 ( $\xi_r = 170^\circ$ ) refer to the ray segments from the core-mantle boundary to the receiver of the *SKS* waves discussed in Section 4. The colour scale is the same for the top and bottom figures.

*SV*-wave sensitivity has the same kind of directional variation as *P*-wave sensitivity, which is asymptotically described by a dependence on the incidence angle and azimuth of the geometrical ray (Fig. 11). The parameters  $L'$  and  $G'$  are the 'horizontal' and 'vertical' parameters for  $o_1$  (Fig. 8). The others parameters are associated with propagation at intermediate angles. The directional dependence causes several sign changes for  $o_1$ -sensitivity to the body-wave parameters  $K'$  and  $D'$ . Similar to *P* waves, amplitude variations may happen for the surface-wave parameters in case of large azimuth variations along the path (Fig. 11). For  $o_2$ , the 'horizontal' parameters are the body-wave parameters  $M'$  (with a high sensitivity) and  $D'$  (Fig. 10). The parameters for which sign changes of the kernel are likely are the surface-wave parameters ( $B'$ ,  $H'$ ,  $G'$  and  $E'$ ) and the body-wave parameters  $D'$ . For strong variations in azimuth along the path, sign changes may occur for  $M'$  and  $K'$ . The observable  $o_1$  for *SV* waves is not sensitive to  $M'$  (Fig. 8). The sensitivity to these parameters (like to the parameter  $N'$ ) is 'turned on' only when *SH* waves are involved. While the  $o_1$ -sensitivity is well described by *SV*-to-*SV* scattering, the observable  $o_2$  corresponds in this case to *SV*-to-*SH* scattering, and it is sensitive to  $M'$  (Fig. 10). *SV* waves are not significantly sensitive to the *P*-wave parameters  $J'$  (Figs 8 and 10). We note, however, numerous small-scale structures with rapid amplitude oscillations for these parameters, but these do not provide constraints on relatively smooth structures (Liu & Tromp 2007).

Concerning transverse isotropy (Fig. 9), the observable  $o_1$  is mainly sensitive to  $\beta_v$  (associated with  $L'$ ). As already noticed by Zhao & Jordan (1998),  $K_{\delta\alpha_h/\alpha_h} \simeq -K_{\delta\alpha_v/\alpha_v}$ , which makes the *SV*-wave observable  $o_1$  not sensitive to  $\alpha$ , and *SV*-wave traveltime anomalies can only constrain the difference  $\alpha_v - \alpha_h$ . The splitting intensity  $o_2$  is virtually unaffected by perturbations in the transversely isotropic (Fig. 10) and isotropic parameters.

### 3.2.3 *SH*-wave adjoint kernels

We next consider pure *SH* waves. The reference isotropic *S* wave is only recorded on the transverse component, therefore,  $s_1(\mathbf{x}_r, t) = 0$  and  $\zeta = 90^\circ$ . The integral definitions (17) and (18) of the observables  $o_1$  and  $o_2$  are thus reduced to

$$o_1 = \frac{1}{N_2} \int \dot{s}_2(\mathbf{x}_r, t) \delta s_2(\mathbf{x}_r, t) dt, \quad (29)$$

$$o_2 = -\frac{1}{N_2} \int \dot{s}_2(\mathbf{x}_r, t) \delta s_1(\mathbf{x}_r, t) dt, \quad (30)$$

with  $N_2 = \int \dot{s}_2^2 dt$ . The relationships (19) and (20) between  $o_1$  and  $o_2$  and the splitting measurements become

$$o_1 = -\frac{1}{2} \Delta T \cos 2\phi - \delta \bar{T}, \quad (31)$$

$$o_2 = -\frac{1}{2} \Delta T \sin 2\phi. \quad (32)$$

The observable  $o_2$  is again the splitting intensity. The observable  $o_1$  is now associated with the opposite of the *SH*-wave traveltime anomaly, since  $o_1 = -\frac{1}{2} \Delta T - \delta \bar{T} = -\delta T_2$  for a transversely isotropic perturbation ( $\phi = 0^\circ$ ).

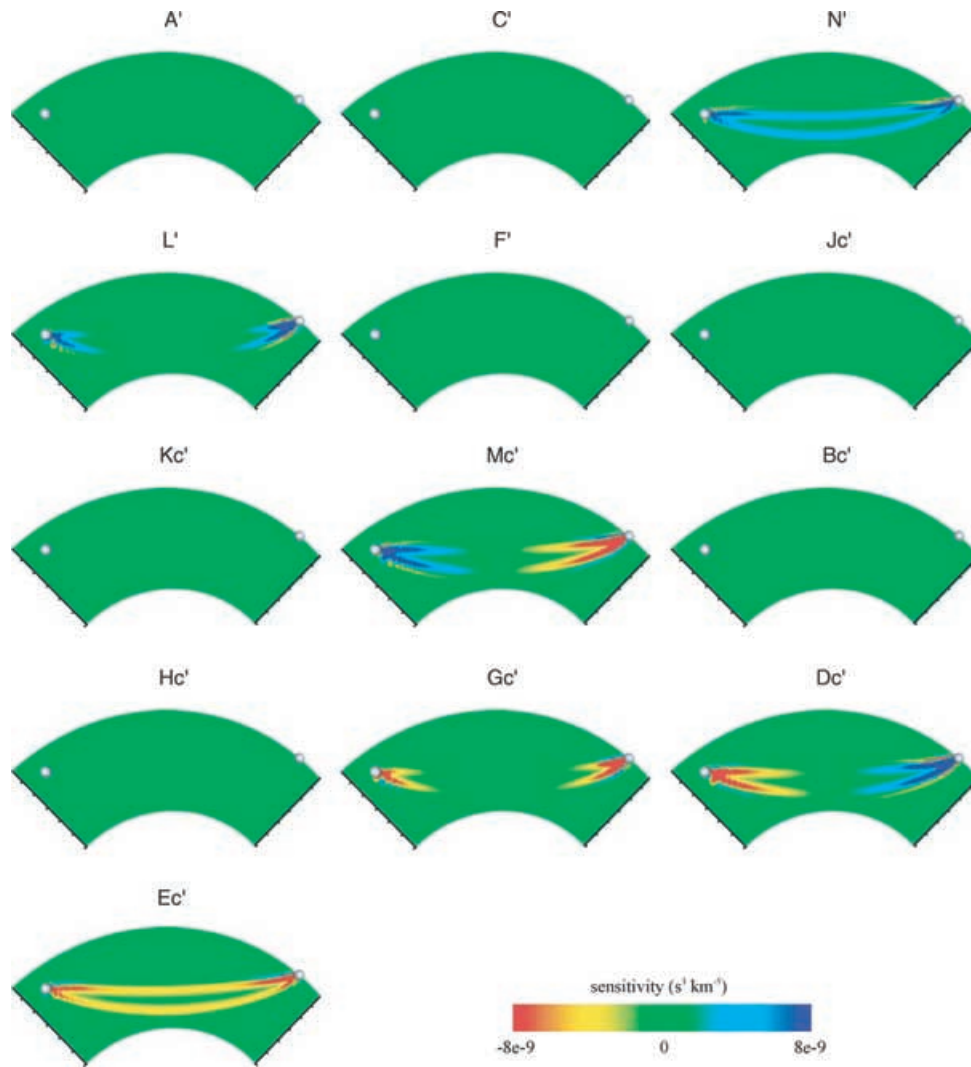


Figure 12. Same as in Fig. 2 but for the *SH*-wave observable  $o_1$  (eq. 31).

The adjoint sensitivity kernels of the *SH*-wave observables  $o_1$  and  $o_2$  are computed for the same source–receiver configuration as before. This time, however, the source mechanism is a point force oriented orthogonally to the source–receiver great-circle plane to produce *S* waves polarized mainly on the transverse component at the receiver. We time-window the *SH*-wave arrival on the transverse component to compute the adjoint source–time function. This adjoint source–time function applied on the transverse component generates the adjoint wavefield necessary to compute the kernels for  $o_1$  (eq. 23), while it is applied on the radial component for  $o_2$  (eq. 24). The adjoint kernels for the Chen & Tromp squared wave speeds are presented in Fig. 12 for  $o_1$  and Fig. 14 for  $o_2$ . In Fig. 13, we show the sensitivity of  $o_1$  to perturbations of the transverse isotropic wave speeds. Like *SV* waves, for *SH* waves it is the observable  $o_1$  that is not sensitive to the *s*-parameters and the splitting intensity  $o_2$  that is not sensitive to the *c*-parameters for this path with a constant azimuth of  $180^\circ$ .

*SH*-wave kernels are simpler than *SV*-wave kernels because there is less ‘contamination’ by converted waves (compare for example Figs 9 and 13). The observable  $o_1$  for *SH* waves is also sensitive to fewer parameters. As predicted by asymptotic theory, there is no sensitivity to perturbations of the *P*-wave parameters  $A'$  and  $C'$ , of the body-wave parameters  $K'$ , and of the surface-wave parameters  $B'$  and  $H'$  (Fig. 12). However, there is sensitivity to the *SH*-wave parameters  $N'$  and  $M'$ . The ‘horizontal’ propagation parameters for  $o_1$  are  $N'$  and  $E'$ , while  $G'$  and  $L'$  are associated with ‘vertical’ propagation. We expect sign changes for  $D'$  and  $M'$ , and for  $G'$  and  $E'$  if the azimuth varies significantly along the path.

For transversely isotropic speeds and  $o_1$  (Fig. 13), *SH* waves are significantly sensitive to  $\beta_h$  for horizontal propagation and to  $\beta_v$  when the propagation direction has a vertical component. Like *P* and *SV* waves, *SH* waves are basically insensitive to a perturbation of the parameter  $\eta$ . Similar to *SV* waves, *SH*-wave sensitivity for  $o_1$  mainly involves *SH*-to-*SH* scattering, while for  $o_2$  it involves *SH*-to-*SV* scattering. Because the observable  $o_2$  retains the same form in terms of the splitting traveltime anomaly  $\Delta T$  and fast polarization angle  $\phi$  for *SV* and *SH* waves, asymptotic theory predicts the same sensitivity for this observable for the two kinds of *S* waves. The adjoint sensitivity kernels in Figs 10 and 14 are indeed alike, although there are some differences due to non-asymptotic propagation effects. We note, especially for the parameters

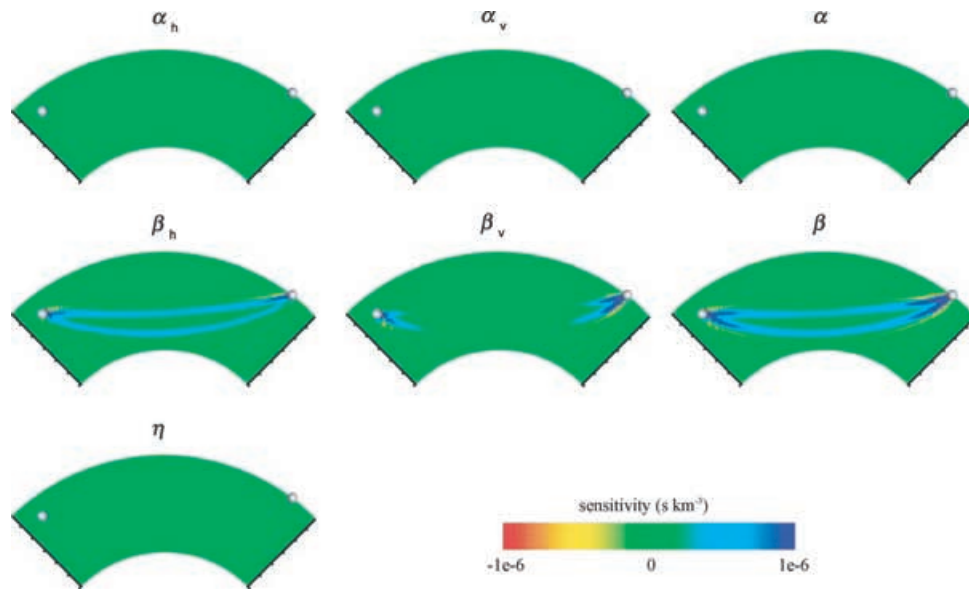


Figure 13. Same as Fig. 3 but for the *SH*-wave observable  $o_1$  (eq. 31), the opposite of the *SH*-wave traveltime anomaly in this case.

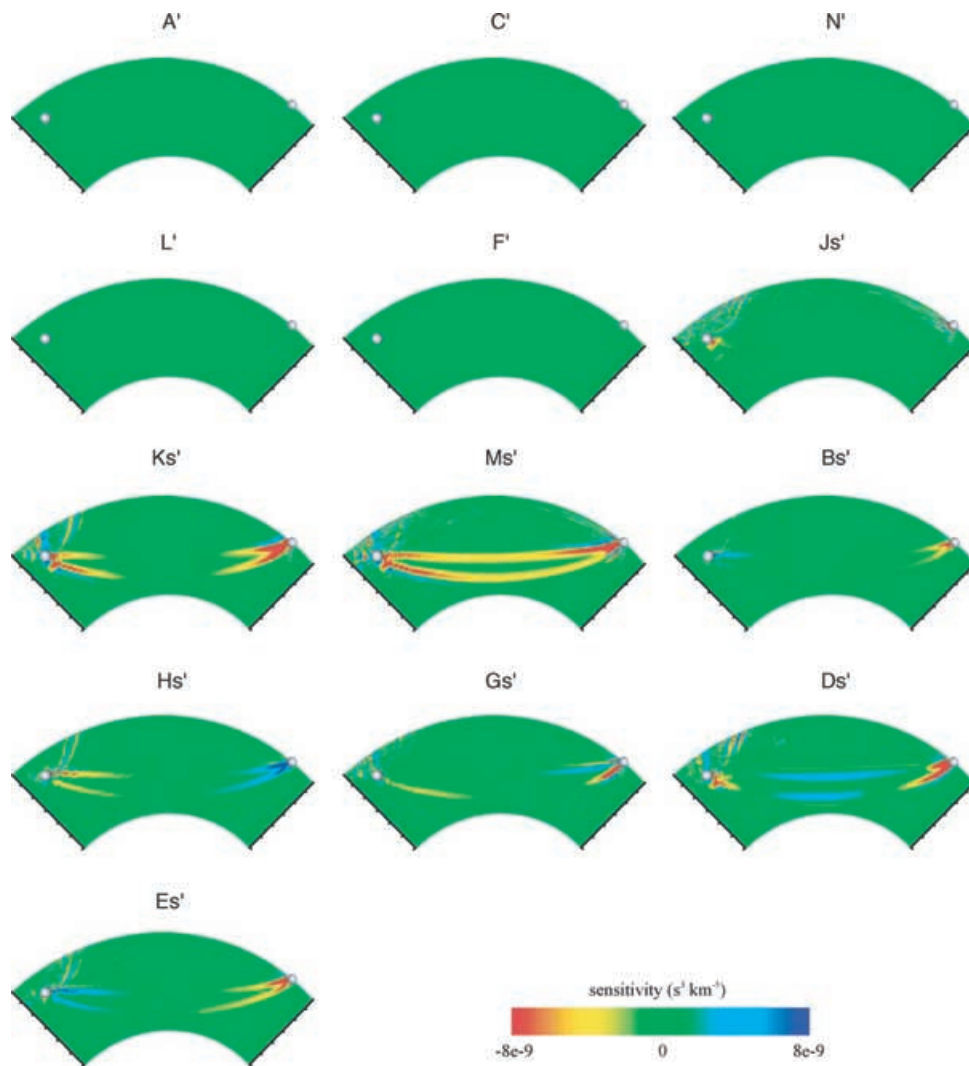
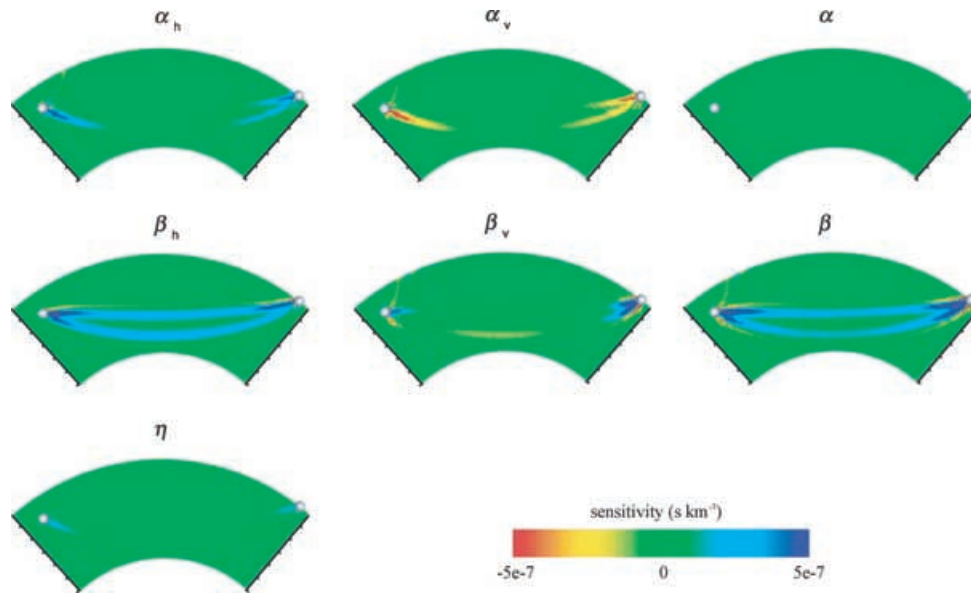


Figure 14. Same as in Fig. 2 but for the *SH*-wave observable  $o_2$  (eq. 32), the splitting intensity.



**Figure 15.** Same as in Fig. 3 but for the  $S$ -wave observable  $o_1$ . The  $S$ -wave kernels are combinations of the  $SV$  (Fig. 9) and  $SH$  kernels (Fig. 14) (eq. 33 with  $a_1 \simeq 0.35$  and  $b_1 \simeq 0.65$  for this experiment). The source mechanism is the 1994 June 9, Bolivia earthquake located at 647 km depth. The colour scale has been divided by two compared to Figs 9 and 14.

$M'$  and  $G'$ , that  $SV$ -wave sensitivity is higher in the upper part of the kernel on the source side and higher in the lower part on the receiver side, while the opposite is true for  $SH$  waves. From a Born theory perspective, this is due to the asymmetry of the scattering coefficients for  $SH$ -to- $SV$  and  $SV$ -to- $SH$  conversions for perturbation of these parameters.

### 3.2.4 General $S$ -wave adjoint kernels

An  $S$ -wave signal can be decomposed into pure  $SV$  and  $SH$  signals (eq. 10). The adjoint sources for  $S$  waves (derived from eqs 17 and 18) are sums of the adjoint sources for pure  $SV$  (eqs 25 and 26) and pure  $SH$  waves (eqs 29 and 30). The  $S$ -wave adjoint kernels  $K^{S_{1,2}}$  for  $o_1$  and  $o_2$  may, therefore, be written as linear combinations of the  $SV$  kernels  $K^{SV_{1,2}}$  and  $SH$  kernels  $K^{SH_{1,2}}$ , for example

$$K^{S_{1,2}} = a_{1,2}K^{SV_1} + b_{1,2}K^{SH_1} + c_{1,2}K^{SV_2} + d_{1,2}K^{SH_2}, \quad (33)$$

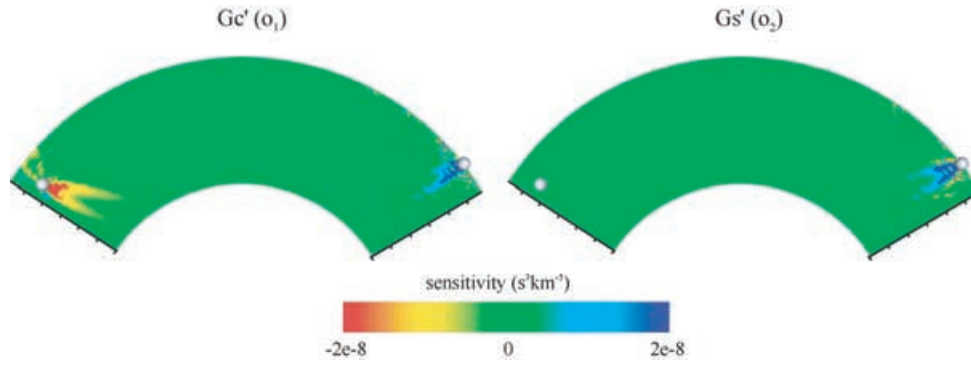
where the coefficients  $a_{1,2}$ ,  $b_{1,2}$ ,  $c_{1,2}$  and  $d_{1,2}$  depend on the observable ( $o_1$  or  $o_2$ ) and the polarization of the reference isotropic shear wave.  $S$ -wave sensitivity can thus be deduced from the previous results for  $SV$  and  $SH$  waves. In general,  $S$ -wave kernels exhibit very complicated patterns with significant sensitivity to all parameters, except the  $P$ -wave parameters  $J'$ .

Fig. 15 shows the sensitivity of the  $S$ -wave observable  $o_1$  to the transversely isotropic wave speeds. The adjoint  $S$ -wave sensitivity kernels are calculated with the same parameters as in the previous experiments (reference model, dominant period of the signal, and epicentral distance), except for the source. We chose the 1994 June 9, Bolivia earthquake located at 647 km depth with a moment magnitude  $M_w = 8.2$ , to generate a clear (full)  $S$ -wave signal at teleseismic distances. We have seen in the previous sections that in the transversely isotropic case  $K^{SV_2} \simeq 0$  and  $K^{SH_2} \simeq 0$ . The kernels  $K^{S_1}$  are thus only a combination of  $K^{SV_1}$  and  $K^{SH_1}$ . For the experiment shown in Fig. 15, the polarization of the reference isotropic shear wave gives  $a_1 \simeq 0.35$  and  $b_1 \simeq 0.65$  in eq. (33), in agreement with the numerical results. Other source mechanisms and paths would however lead to different values of these coefficients.

These experiments with teleseismic direct  $P$  and  $S$  waves paint the general picture of body-wave sensitivity to anisotropy. In the next section we explore the specific example of  $SKS$  waves, which are widely used to constrain anisotropy.

## 4 SKS SENSITIVITY

$SKS$  waves start as  $S$  waves (generally polarized along both the  $SV$  and  $SH$  directions) at the source. They are converted to  $P$  waves when entering the liquid outer core, and then emerge out of the core back into the mantle as  $SV$  waves with a near-vertical propagation direction. In an isotropic model, they only appear on the vertical and radial components at the receiver. For  $SKS$ , the integral definitions of the observables  $o_1$  and  $o_2$  (eqs 17 and 18) reduce to the definitions for  $SV$  waves governed by eqs (25) and (26) ( $s_2 = 0$ ). If we identify the  $SV$ - and  $SH$ -directions with the radial and transverse components, the observable  $o_1$  reflects the perturbation of the radial component, while  $o_2$  measures the perturbation of the transverse component. When the anisotropic perturbation is situated on the receiver side, we are in a pure  $SV$ -wave situation. The observable  $o_1$  is then a generalized traveltime anomaly  $-\frac{1}{2}\Delta T \cos 2\phi + \delta\bar{T}$ , and the observable  $o_2$  is the splitting intensity  $-\frac{1}{2}\Delta T \sin 2\phi$ . When the anisotropic perturbation is located between the source and the core–mantle boundary (CMB), before entering the



**Figure 16.** Adjoint sensitivity kernels of an *SKS* wave with a dominant period of 15 s for the generalized traveltime anomaly  $o_1$  (eq. 17) and the parameter  $G'_c$  (left-hand side), and for the splitting intensity  $o_2$  (eq. 18) and the parameter  $G'_s$  (right-hand side). The epicentral distance is  $105^\circ$ , the azimuth at the receiver,  $\xi_r$ , is  $99^\circ$ , and the source is the Bolivia earthquake located at 647 km depth.

core, it is a full *S* wave (*SV* and *SH* polarized) that hits the anisotropic perturbation. The splitting phenomenon transfers *SV* signal to the *SH* component as well as *SH* signal to the *SV* component according to eq. (14). The propagation through the core prevents any *SH* signal to reach the receiver, and thus the observed signal is of the form

$$\mathbf{d}(\mathbf{x}_r, t) \simeq \left[ s_1(\mathbf{x}_r, t) - \delta\bar{T} \dot{s}_1(\mathbf{x}_r, t) + \frac{1}{2} \Delta T \cos 2\phi \dot{s}_1(\mathbf{x}_r, t) + \frac{1}{2} \Delta T \sin 2\phi \dot{\bar{s}}_2(\mathbf{x}_r, t) \right] \hat{\mathbf{e}}_1. \quad (34)$$

The quantity  $\bar{s}_2(\mathbf{x}_r, t)$  is not a simple *SH* signal observed at the receiver on the transverse component similar to eq. (14). It is the *SH* signal emitted by the source that has subsequently undergone *SV*-wave propagation from the anisotropic perturbation to the receiver. The relationship between the observable  $o_1$  and the splitting parameters is in this case

$$o_1 = -\frac{1}{2} \Delta T \cos 2\phi + \delta\bar{T} - \frac{1}{4} \Delta T \sin 2\phi \sin 2\zeta. \quad (35)$$

The splitting intensity  $o_2$  is zero in this case, reflecting the fact that the *SKS*-splitting intensity is not sensitive to perturbations encountered before propagating through the core. The observable  $o_1$ , however, is affected by such perturbations. The splitting intensity  $-\frac{1}{2} \Delta T \sin 2\phi$  appears in eq. (35) weighted by a quantity depending on the polarization of the reference isotropic *S* wave (angle  $\zeta$ ). We therefore, expect *SKS* sensitivity for  $o_1$  to display the characteristics of the *SV*-wave sensitivity for the splitting intensity between the source and the CMB superimposed on the *SV*-wave sensitivity pattern for  $o_1$ .

We compute the adjoint sensitivity kernels associated with the *SKS* observables  $o_1$  and  $o_2$  using the source mechanism of the Bolivia earthquake to generate clear *SKS* waves. The reference model is again isotropic PREM. The epicentral distance is  $105^\circ$ , so that the *SKS* pulse is clearly separated from other arrivals. The spectral-element simulation is accurate for periods longer than 14.5 s. A dominant period of 14.5 s for the signal is appropriate, since this is about 10 times larger than the usually observed split time  $\Delta T$  (Savage 1999) and is within the typical period range for *SKS* studies (Schulte-Pelkum & Balckman 2003).

In Fig. 16, we present the sensitivity of the observable  $o_1$  to the parameter  $G'_c$  and of the observable  $o_2$  to the parameter  $G'_s$ . The adjoint kernel for  $o_1$  agrees with asymptotic predictions. Unlike the *SKS*-splitting intensity (Fig. 16, right-hand side), the *SKS* observable  $o_1$  ‘remembers’ the propagation and constrains the structure before entering the core (Fig. 16, left-hand side), in agreement with its interpretation as a traveltime observable.

We now focus on the sensitivity of the *SKS*-splitting intensity, an observable that is being used to map mantle anisotropy (e.g. Chevrot 2006; Long & van der Hilst 2005). Fig. 17 zooms in on the receiver side of the adjoint kernels for the Chen & Tromp squared wave speeds for a  $105^\circ$  path whose geographical coordinates are different from the path used in Fig. 16. We focus on the *s*-parameters, since the *c*-parameter kernels exhibit the same sensitivity patterns. Like for *SV* waves, the *SKS*-splitting intensity is insensitive to the transversely isotropic parameters and to the isotropic wave speeds. This is a confirmation of previous work (e.g. Chevrot 2006). Only azimuthal anisotropy matters to this observable. The sensitivity of the *SKS*-splitting intensity exhibits the typical *SV*-wave directional dependence, but with some particularities controlled by the specific *SKS* path-geometry.

The first particularity is that the *SKS*-splitting intensity is not sensitive to perturbations encountered before entry into the core (Fig. 16), as generally assumed and discussed earlier. *SKS* propagation is nearly vertical on the receiver side. For such incidence angles (Fig. 11), the splitting intensity is only significantly sensitive to the four pairs of azimuthal parameters  $K'$ ,  $M'$ ,  $G'$  and  $D'$  (Fig. 17). *SKS*-splitting measurements are usually interpreted by assuming transverse isotropy with a horizontal symmetry axis. The description of such a structure with the Chen & Tromp parameters involves the transversely isotropic and surface-wave parameters ( $A$ ,  $C$ ,  $F$ ,  $L$ ,  $N$ ,  $B$ ,  $H$ ,  $G$  and  $E$ ) (Section B2 of Appendix B). If the structure is transversely isotropic with a horizontal symmetry axis, the only relevant parameters for the *SKS*-splitting intensity are, therefore, the parameters  $G'$ . The high sensitivity close to the receiver for these parameters is due to the combined effects of geometrical focusing and the scattering coefficient via the asymptotic directional dependence (Fig. 11). Favier *et al.* (2004) showed that near-field effects are also important to model finite-frequency *SKS* splitting. The directional dependence is not as obvious as it was for direct

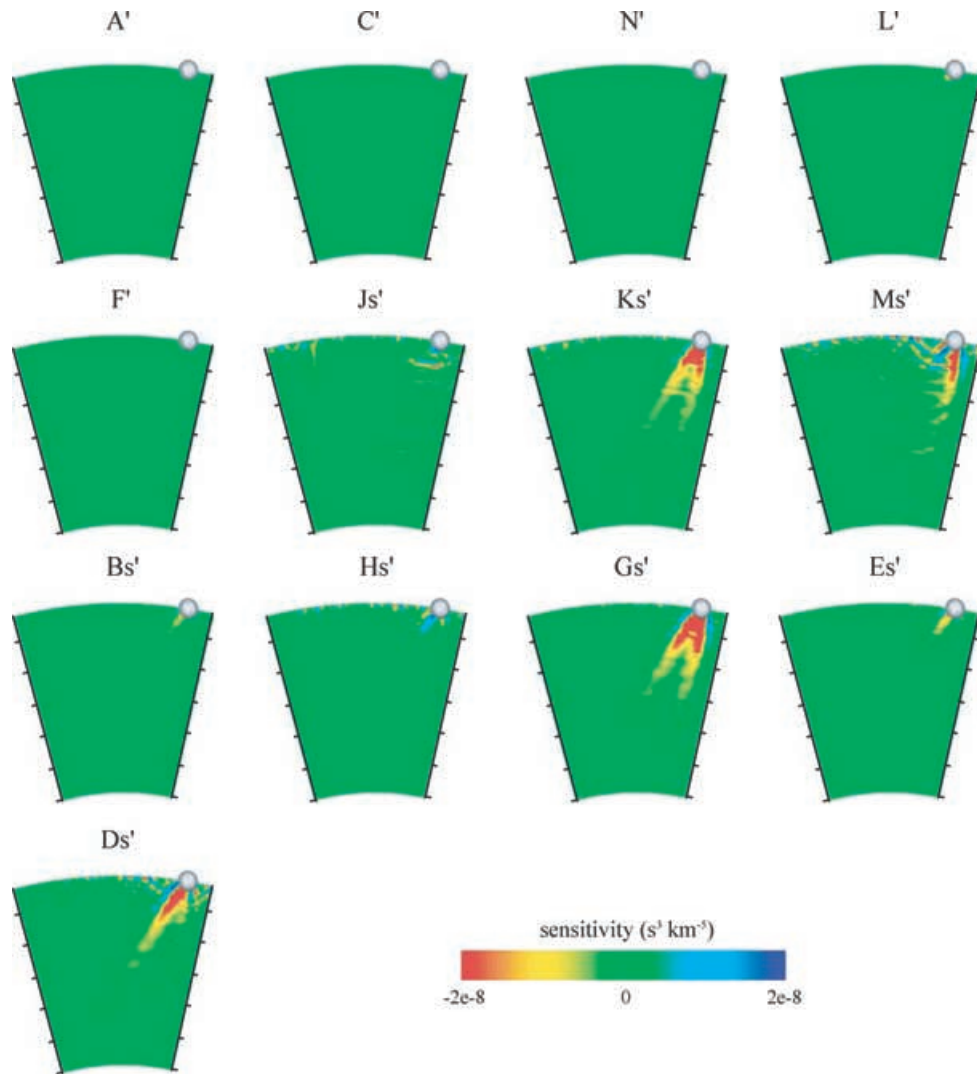


**Figure 17.** Zoom-ins on the receiver region from the CMB to the surface of the *SKS* adjoint sensitivity kernels for the splitting intensity  $o_2$  and 13 of the Chen & Tromp squared wave speeds. The sensitivity is significant for  $G'_s$ ,  $K'_s$ ,  $M'_s$  and  $D'_s$ . The epicentral distance is  $105^\circ$  and the azimuth at the receiver,  $\xi_r$ , is  $170^\circ$ . The dominant period of the signal is about 15 s. The tick marks of the depth scale are again situated every 500 km from the core–mantle boundary to the surface, that is, the first and second tick marks from the surface are at 400 and 900 km depth, respectively.

SV waves (Fig. 10). We do not observe sign changes of the kernel amplitude in Fig. 17. This is related to the small variations of both incidence angle and azimuth along the geometrical ray from the CMB to the receiver (Fig. 11). For a  $105^\circ$  path, which corresponds to an average epicentral distance for *SKS*-splitting studies (e.g. Silver & Chan 1988), the incidence angle varies from  $30^\circ$  at the CMB to  $8^\circ$  at the surface. The local azimuth varies between  $104^\circ$  and  $99^\circ$  along the path shown in Fig. 16 from the CMB to the surface, and between  $162^\circ$  and  $170^\circ$  for the path shown in Fig. 17. We see, however, that the local azimuths may be quite different from one path to another. This makes the sensitivity very path-dependent, as is illustrated in Fig. 18, which compares the sensitivity to  $G'_s$  for two paths with the same length ( $105^\circ$ ) but with different geographical coordinates (different receiver locations).

With a dominant period of about 15 s, for the parameter  $G'_s$  the high-sensitivity zone (the red or dark blue regions) reaches 700 km depth with a width of about 500 km for the two  $105^\circ$  paths (Figs 17 and 18). The depth extent of the sensitivity zone is determined by geometrical focusing and near-field effects, but the directional dependence also has some influence. The asymptotic formulation allows us to identify the two  $105^\circ$  paths as end-members with regards to the azimuthal dependence. The asymptotic sensitivity of the *SKS*-splitting intensity to  $G'_s$  is indeed  $\cos 2\xi$ -dependent. For the two paths the local azimuth in the vicinity of the receiver,  $\xi_r$ , is close to  $90^\circ$  or  $180^\circ$  (Fig. 11). When  $\xi_r$  is close to  $45^\circ$  or  $135^\circ$ , we predict a shallower sensitivity zone. The sensitivity of the *SKS*-splitting intensity to  $G'_c$  is  $\sin 2\xi$ -dependent, and therefore, deeper when  $\xi_r$  is  $45^\circ$  or  $135^\circ$  and shallower when  $\xi_r$  is  $90^\circ$  or  $180^\circ$ , as shown in Fig. 18. For an azimuth at the receiver of  $170^\circ$  and a period of about 15 s, the significant sensitivity extends down to only 400 km for  $G'_c$ . This corresponds to the maximum depth usually considered for anisotropy detected by *SKS*-splitting measurements (Alsina & Snieder 1995; Silver 1996). The depth extent of the sensitivity zone is also controlled by the incidence angle along the path. The more vertical the path, the higher the sensitivity. As discussed in Section 3.1, decreasing the wave period will make the sensitivity zone narrower and the overall amplitude higher. However, the directional dependence

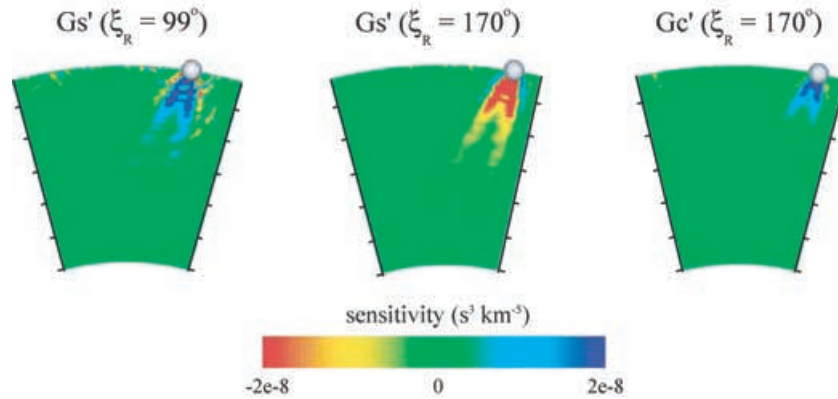


**Figure 18.** Comparison between the sensitivity of the *SKS*-splitting intensity to the parameter  $G'_s$  for the path shown in Fig. 16 with  $\xi_r = 99^\circ$  (left-hand side) and the path shown in Fig. 17 with  $\xi_r = 170^\circ$  (middle). Free-surface effects are clearly visible for the path on the left-hand side. The significant sensitivity zone extends down to the transition zone ( $\sim 700$  km depth), but these two paths are end-members (Fig. 11). A sensitivity slightly shallower would be obtained for other paths, as observed for the parameter  $G'_c$  for the path with  $\xi_r = 170^\circ$  (right-hand side), where the high-sensitivity zone does not extend below 400 km.

will be unchanged and the same focusing of sensitivity at ‘shallow’ depths beneath the receiver should be observed at shorter periods. We note that for epicentral distances within the recommended range ( $85^\circ$ – $110^\circ$ , Silver & Chan 1988), the *SKS*-splitting intensity is not significantly sensitive to the  $D''$  region.

An additional feature is observed for the path shown in Fig. 16 (or Fig. 18, left-hand side). The sensitivity involves numerous structures off the first Fresnel zone, such as the circular patterns at different depths. Following Hung *et al.* (2000) and Zhao & Jordan (2006), we repeated the experiment for a model in which we replaced PREM by a smooth mantle model without wave speed discontinuities nor gradients. Although the kernels computed in this smoothed model are slightly simpler, the major circular structures remain. This suggests that these structures are likely caused by reverberations at the free surface. They are due to  $P$  and  $S$  waves reflected at the free surface from incident *SKP* waves that are backscattered in the mantle and arrive at the receiver in the selected *SKS* time window, that is, *SKPP* and *SKPS*. Computations with other epicentral distances give similar patterns, which are also observed for the sensitivity of the *SV* traveltime anomaly to the isotropic shear-wave speed  $\beta$  (Liu & Tromp 2007).

## 5 DISCUSSION AND CONCLUSION

Using the adjoint spectral-element method, we have investigated the sensitivity of finite-frequency body waves to the 21 elastic parameters naturally involved in the asymptotic description of seismic wave propagation in weakly anisotropic media. Overall, we retrieve the ‘banana-doughnut’ pattern widely found for isotropic parameters. Compared to the isotropic case, the main characteristic of body-wave sensitivity to anisotropy is a strong path dependence, resulting in large amplitude variations and, for azimuthal parameters, even sign changes. This pattern is asymptotically explained by a dependence on the incidence angle and the azimuth of propagation.

A particularly notable feature of  $P$ -wave cross-correlation traveltime anomalies is their high sensitivity to a perturbation of the parameters  $J'_{c,s}$  associated with  $1-\xi$  azimuthal variations.  $P$ -wave sensitivity to these parameters is one order of magnitude larger than for the transversely isotropic parameters, from which the isotropic wave speeds are derived. Only materials with low-order symmetry (monoclinic and triclinic systems) have non-zero  $J'_{c,s}$  in the material’s natural coordinates (Babuška & Cara 1991). However, in general the coordinates we use do not correspond to the symmetry axes of the material. For example,  $J'_{c,s}$  are not zero for a transversely isotropic structure with a tilted symmetry axis. This explains Sobolev *et al.*’s (1999) synthetic experiments showing significant artefacts in isotropic  $P$ -wave tomography due to anisotropic bodies with a dipping symmetry axis, such as subduction zones. If large-scale alignment is to be expected in the mantle, isotropic traveltime anomalies could be substantially biased.

To analyse  $S$ -wave sensitivity to anisotropy, we have defined two new observables, because shear-wave splitting makes the traditional cross-correlation traveltime anomaly not an appropriate measure. The first observable we propose is a generalized cross-correlation traveltime anomaly, while the second observable is a generalized splitting intensity. Like  $P$  waves,  $S$  waves analysed based upon these observables are generally sensitive to a large number of the 21 anisotropic parameters. This suggests that the parametrization of anisotropy used here may not be optimal for imaging. It would be difficult to conduct a tomographic inversion for such a large number of model parameters. Other parametrizations may be more advantageous, like for example parametrizations based on a priori knowledge of the anisotropic properties of Earth materials (Becker *et al.* 2006; Chevrot 2006).

For *SKS* waves, the second  $S$ -wave observable simplifies to the ‘splitting intensity’ introduced and developed by Chevrot (2000, 2006). The specific path-geometry of *SKS* waves makes the *SKS*-splitting intensity interesting for imaging. This observable is only sensitive to a limited number of anisotropic parameters compared to  $P$  and  $S$  waves or Rayleigh waves (Sieminski *et al.* 2007). The region of significant sensitivity is also relatively confined. It is located beneath the receiver, extending with some directional-dependence down to transition-zone

depths. It is quite different from the surface-wave sensitivity zone (Sieminski *et al.* 2007), explaining the usual poor correlation between surface-wave and *SKS*-splitting studies (Montagner *et al.* 2000). Because *SKS* splitting samples the mantle deeper than fundamental-mode surface waves at intermediate periods, it seems interesting to combine surface-wave data and *SKS*-splitting measurements to better constrain the anisotropic structure of the transition zone, for example. Measurements of the splitting intensity for teleseismic *S* waves are sometimes used to complement *SKS*-data sets (e.g. Savage 1999; Long & van der Hilst 2005). We cannot compute adjoint sensitivity kernels for the *S*-wave splitting intensity. However, from the analysis of the *S*-wave generalized splitting intensity, we expect *S*-wave splitting intensity to be sensitive to structure all along the ray path. This may bias the results when using *S*-wave splitting to constrain anisotropy beneath the receiver.

The sensitivity of the *SKS*-splitting intensity has previously been described by the formulation of Favier & Chevrot (2003) and Favier *et al.* (2004). They applied Born-scattering theory with a plane-wave description and focused on the sensitivity to two perturbation parameters. These parameters are directly related to the parameters we used in this study (Section B2), so that the results can be compared. Working with plane waves misses the effects of variations of the incidence angle and azimuth along the path that partly control the sensitivity pattern (i.e. the depth extent of the significant sensitivity zone), and it is also difficult to model free-surface effects. It is not clear yet whether these limitations are significant for imaging. A full-wave approach, such as the adjoint spectral-element method, naturally models all these effects, as well as the near field, which makes the technique, therefore, very promising for significant progress in anisotropic imaging.

## ACKNOWLEDGMENTS

We thank Sonja Greve, Martha Savage, an anonymous reviewer and editor Cindy Ebinger for helpful comments and suggestions. The adjoint spectral-element computations discussed in this paper were performed on Caltech's Division of Geological & Planetary Sciences Dell cluster. The source code for the adjoint spectral-element simulations is freely available from [www.geodynamics.org](http://www.geodynamics.org). We gratefully acknowledge support from the European Commission's Human Resources and Mobility Programme, Marie Curie Research Training Networks, FP6 and by the National Science Foundation under grant EAR-0309576. This is contribution no 9170 of the Division of Geological & Planetary Sciences of the Californian Institute of Technology.

## REFERENCES

- Alsina, D. & Snieder, R., 1995. Small-scale sublithospheric continental mantle deformation: constraints from *SKS* splitting observations, *Geophys. J. Int.*, **123**, 431–448.
- Babuška, V. & Cara, M., 1991. *Seismic Anisotropy in the Earth*, Kluwer Academic, Dordrecht.
- Becker, T.W., Chevrot, S., Schulte-Pelkum, V. & Blackman, D.K., 2006. Statistical properties of seismic anisotropy predicted by upper mantle geodynamic models, *J. geophys. Res.*, **111**, B08309, doi:10.1029/2005JB004095.
- Calvet, M., Chevrot, S. & Souriau, A., 2006. *P*-wave propagation in transversely isotropic media I. Finite-frequency theory, *Phys. Earth planet. Int.*, **156**, 12–20.
- Chen, M. & Tromp, J., 2007. Theoretical and numerical investigation of global and regional seismic wave propagation in weakly anisotropic Earth models, *Geophys. J. Int.*, **168**, 1130–1152.
- Chevrot, S., 2000. Multichannel analysis of shear wave splitting, *J. geophys. Res.*, **105**, 21 579–21 590.
- Chevrot, S., 2006. Finite-frequency vectorial tomography: a new method for high resolution imaging of mantle anisotropy, *Geophys. J. Int.*, **165**, 641–657.
- Dahlen, F.A., Hung, S.-H. & Nolet, G., 2000. Fréchet kernels for finite-frequency traveltimes-I. Theory, *Geophys. J. Int.*, **141**, 157–174.
- Dziewonski, A.M. & Anderson, D.L., 1981. Preliminary Reference Earth Model, *Phys. Earth planet. Inter.*, **25**, 297–356.
- Farra, V., 2001. High-order perturbations of the phase velocity and polarization of *qP* and *qS* waves in anisotropic media, *Geophys. J. Int.*, **147**, 93–104.
- Favier, N. & Chevrot, S., 2003. Sensitivity kernels for shear wave splitting in transverse isotropic media, *Geophys. J. Int.*, **153**, 213–228.
- Favier, N., Chevrot, S. & Komatitsch, D., 2004. Near-field influence on shear wave splitting and traveltime sensitivity kernels, *Geophys. J. Int.*, **156**, 467–482.
- Grésillaud, A. & Cara, M., 1996. Anisotropy and *P*-wave tomography: a new approach for inverting teleseismic data from a dense array of stations, *Geophys. J. Int.*, **126**, 77–91.
- Hess, H.H., 1964. Seismic anisotropy of the uppermost mantle under oceans, *Nature*, **203**, 629–631.
- Hung, S.-H., Dahlen, F.A. & Nolet, G., 2000. Fréchet kernels for finite-frequency traveltimes-II. Examples, *Geophys. J. Int.*, **141**, 175–203.
- Jech, J. & Pšenčík, I., 1989. First-order perturbation method for anisotropic media, *Geophys. J. Int.*, **99**, 369–376.
- Kaminski, É. & Ribe, N.L.M., 2002. Timescales for the evolution of seismic anisotropy in mantle flow, *Geochem. Geophys. Geosyst.*, **3**(1), 10.1029/2001GC000222.
- Komatitsch, D. & Vilotte, J.P., 1998. The spectral-element method: an efficient tool to simulate the seismic response of 2D and 3D geological structures, *Bull. seism. Soc. Am.*, **88**(2), 368–392.
- Komatitsch, D. & Tromp, J., 2002a. Spectral-element simulations of global seismic wave propagation-I. Validation, *Geophys. J. Int.*, **149**, 390–412.
- Komatitsch, D. & Tromp, J., 2002b. Spectral-element simulations of global seismic wave propagation-II. Three-dimensional models, oceans, rotation and self-gravitation, *Geophys. J. Int.*, **150**, 303–318.
- Larson, E., Tromp, J. & Ekström, G., 1998. Effects of slight anisotropy on surface waves, *Geophys. J. Int.*, **132**, 654–666.
- Liu, Q. & Tromp, J., 2006. Finite-frequency kernels based upon adjoint methods, *Bull. seism. Soc. Am.*, **96**, 2383–2397.
- Liu, Q. & Tromp, J., 2007. Finite-frequency sensitivity kernels for global seismic wave propagation based upon adjoint methods, *Geophys. J. Int.*, in preparation.
- Long, M.D. & van der Hilst, R.D., 2005. Estimating shear-wave splitting parameters from broadband recordings in Japan: a comparison of three methods, *Bull. seism. Soc. Am.*, **95**, 1346–1358.
- Love, A.E.H., 1911. *Some Problems of Geodynamics*, Cambridge University Press, Cambridge.
- Mainprice, D., Barruol, G. & Ben Ismail, W., 2000. The seismic anisotropy of the Earth's mantle: from single crystal to polycrystal, *Geophys. Monograph*, **117**, 237–264.
- Marquering, H., Dahlen, F.A. & Nolet, G., 1999. Three-dimensional sensitivity kernels for finite-frequency traveltimes: the banana-doughnut paradox, *Geophys. J. Int.*, **137**, 805–815.
- Montagner, J.P. & Nataf, H.C., 1986. A simple method for inverting the azimuthal anisotropy of surface waves, *J. geophys. Res.*, **91**, 511–520.
- Montagner, J.P., Griot-Pommeroy, D.A. & Lavé, J., 2000. How to relate body wave and surface wave anisotropy?, *J. geophys. Res.*, **105**, 19 015–19 027.
- Plomerová, J., Šílený, J. & Babuška, V., 1996. Joint interpretation of upper-mantle anisotropy based on teleseismic *P*-travel time delays and inversion

- of shear-wave splitting parameters, *Phys. Earth. planet. Int.*, **95**, 293–309.
- Press, W., Teukolsky, S., Vetterling, W. & Flannery, B., 1992. *Numerical Recipes in FORTRAN: The Art of Scientific Computing*, Cambridge University Press, Cambridge.
- Savage, M.K., 1999. Seismic anisotropy and mantle deformation: what have we learned from shear wave splitting?, *Rev. Geophys.*, **37**, 65–106.
- Schulte-Pelkum, V. & Balckman, D.K., 2003. A synthesis of seismic P and S anisotropy, *Geophys. J. Int.*, **154**, 166–178.
- Silver, P.G., 1996. Seismic anisotropy beneath the continents: Probing the depths of geology, *Annu. Rev. Earth Planet. Sci.*, **24**, 385–432.
- Silver, P.G. & Chan, W.W., 1988. Implications for continental structure and evolution from seismic anisotropy, *Nature*, **335**, 34–39.
- Sieminski, A., Liu, Q., Trampert, J. & Tromp, J., 2007. Finite-frequency sensitivity of surface waves to anisotropy based upon adjoint methods, *Geophys. J. Int.*, **168**, 1153–1174.
- Smith, M.L. & Dahlen, F.A., 1973. The azimuthal dependence of Love and Rayleigh wave propagation in a slightly anisotropic medium, *J. geophys. Res.*, **78**, 3321–3333.
- Sobolev, S.V., Grésillaud, A. & Cara, M., 1999. How robust is isotropic delay time tomography for anisotropic mantle?, *Geophys. Res. Lett.*, **26**, 509–512.
- Tape, C., Liu, Q. & Tromp, J., 2007. Finite frequency tomography using adjoint methods—methodology and examples using membrane surface waves, *Geophys. J. Int.*, **168**, 1105–1129.
- Tarantola, A., 1984. Inversion of seismic reflection data in acoustic approximation, *Geophysics*, **49**, 1259–1266.
- Tarantola, A., 1987. Inversion of travel times and seismic waveforms, in *Seismic Tomography*, pp. 135–157, ed. Nolet G., Reidel, Dordrecht.
- Tarantola, A., 1988. Theoretical background for the inversion of seismic waveforms, including elasticity and attenuation, *Pure appl. Geophys.*, **128**, 365–399.
- Tromp, J., Tape, C. & Liu, Q., 2005. Seismic tomography, adjoint methods, time reversal and banana-doughnut kernels, *Geophys. J. Int.*, **160**, 195–216.
- Vinnik, L.P., Farra, V. & Romanowicz, B., 1989. Azimuthal anisotropy in the Earth from observations of SKS at Geoscope and NARS broadband stations, *Bull. seism. Soc. Am.*, **79**, 1542–1558.
- Wessel, P. & Smith, W.H.F., 1995. New version of the Generic Mapping Tools released, *EOS Trans. Am. geophys. Un.*, **76**, 329.
- Zhao, L. & Jordan, T.H., 1998. Sensitivity of frequency-dependent travel-times to laterally heterogeneous, anisotropic Earth structure, *Geophys. J. Int.*, **133**, 683–704.
- Zhao, L. & Jordan, T.H., 2006. Structural sensitivities of finite-frequency seismic waves: a full-wave approach, *Geophys. J. Int.*, **165**, 981–990.
- Zhao, L., Jordan, T.H., Olsen, K.B. & Chen, P., 2005. Fréchet kernels for imaging regional Earth structure based on three-dimensional reference models, *Bull. seism. Soc. Am.*, **95**, 2066–2080.
- Zhou, Y., Liu, Q. & Tromp, J., 2006. Finite-frequency surface wave sensitivity kernels for 3-D earth models, *EOS, Trans. Am. geophys. Un.*, **87**(52), Fall Meet. Suppl.

## APPENDIX A: ANISOTROPIC ELASTIC PARAMETERS

The 21 elastic parameters  $C_{IJ}$ ,  $I, J = 1, \dots, 6$ , using Voigt's notation with contracted indices, are related to the elements of the elastic tensor  $c_{ijkl}$ ,  $i, j, k, l = 1, 2, 3$ , in spherical coordinates ( $\hat{\mathbf{r}}$  pointing upward,  $\hat{\boldsymbol{\theta}}$  to the South, and  $\hat{\boldsymbol{\phi}}$  to the East) by

$$\begin{pmatrix} C_{11} & C_{12} & C_{13} & C_{14} & C_{15} & C_{16} \\ & C_{22} & C_{23} & C_{24} & C_{25} & C_{26} \\ & & C_{33} & C_{34} & C_{35} & C_{36} \\ & & & C_{44} & C_{45} & C_{46} \\ & & & & C_{55} & C_{56} \\ & & & & & C_{66} \end{pmatrix} = \begin{pmatrix} c_{\theta\theta\theta\theta} & c_{\theta\theta\phi\phi} & c_{\theta\theta rr} & c_{\theta\theta\phi r} & c_{\theta\theta\theta r} & c_{\theta\theta\theta\phi} \\ & c_{\phi\phi\phi\phi} & c_{\phi\phi rr} & c_{\phi\phi\phi r} & c_{\phi\phi\theta r} & c_{\phi\phi\theta\phi} \\ & & c_{rrrr} & c_{rr\phi r} & c_{rr\theta r} & c_{rr\theta\phi} \\ & & & c_{\phi r\phi r} & c_{\phi r\theta r} & c_{\phi r\theta\phi} \\ & & & & c_{\theta r\theta r} & c_{\theta r\theta\phi} \\ & & & & & c_{\theta\phi\theta\phi} \end{pmatrix}. \quad (\text{A1})$$

The 21 anisotropic elastic parameters of Chen & Tromp (2007) are given in terms of these parameters by the following relations

$$A = \frac{1}{8}(3C_{11} + 3C_{22} + 2C_{12} + 4C_{66}),$$

$$C = C_{33},$$

$$N = \frac{1}{8}(C_{11} + C_{22} - 2C_{12} + 4C_{66}),$$

$$L = \frac{1}{2}(C_{44} + C_{55}),$$

$$F = \frac{1}{2}(C_{13} + C_{23}),$$

$$J_c = \frac{1}{8}(3C_{15} + C_{25} + 2C_{46}),$$

$$J_s = \frac{1}{8}(C_{14} + 3C_{24} + 2C_{56}),$$

$$K_c = \frac{1}{8}(3C_{15} + C_{25} + 2C_{46} - 4C_{35}),$$

$$K_s = \frac{1}{8}(C_{14} + 3C_{24} + 2C_{56} - 4C_{34}),$$

$$M_c = \frac{1}{4}(C_{15} - C_{25} + 2C_{46}),$$

$$M_s = \frac{1}{4}(C_{14} - C_{24} - 2C_{56}),$$

$$G_c = \frac{1}{2}(C_{55} - C_{44}),$$

$$\begin{aligned}
G_s &= -C_{45}, \\
B_c &= \frac{1}{2}(C_{11} - C_{22}), \\
B_s &= -(C_{16} + C_{26}), \\
H_c &= \frac{1}{2}(C_{13} - C_{23}), \\
H_s &= -C_{36}, \\
D_c &= \frac{1}{4}(C_{15} - C_{25} - 2C_{46}), \\
D_s &= \frac{1}{4}(C_{14} - C_{24} + 2C_{56}), \\
E_c &= \frac{1}{8}(C_{11} + C_{22} - 2C_{12} - 4C_{66}), \\
E_s &= -\frac{1}{2}(C_{16} - C_{26}).
\end{aligned} \tag{A2}$$

## APPENDIX B: TRANSVERSE ISOTROPY

Transverse isotropy is the simplest kind of anisotropy. It corresponds to an anisotropic material exhibiting hexagonal symmetry, that is, the elastic properties of the material are invariant when rotated around one single direction in space (Babuška & Cara 1991). There are only five independent elastic coefficients. In the next two sections we will consider transverse isotropy with vertical and horizontal symmetry axes, respectively.

### B1 Vertical symmetry axis

Transverse isotropy with a vertical (or radial) symmetry axis is sometimes called radial anisotropy. A horizontally layered structure is an example of such a model. In this structure, the speeds of horizontally propagating  $P$  waves ( $\alpha_h$ ), vertically propagating  $P$  waves ( $\alpha_v$ ), horizontally propagating  $S$  waves ( $\beta_h$ ) and of vertically propagating  $S$  waves ( $\beta_v$ ) are simply related to the Chen & Tromp parametrization (Appendix A). To complete the model description based upon wave speeds, an additional parameter  $\eta$  is needed. It is involved in wave propagation at intermediate incidence angles. We have the following relations:

$$\alpha_h = \sqrt{\frac{A}{\rho}}, \quad \alpha_v = \sqrt{\frac{C}{\rho}}, \quad \beta_h = \sqrt{\frac{N}{\rho}}, \quad \beta_v = \sqrt{\frac{L}{\rho}}, \quad \eta = \frac{F}{A - 2L}. \tag{B1}$$

The sensitivity kernels for relative perturbations of these parameters are combinations of the kernels for the Chen & Tromp parameters:

$$K_{\delta\alpha_h/\alpha_h} = 2AK_{\delta A} + 2A\eta K_{\delta F}, \quad K_{\delta\alpha_v/\alpha_v} = 2CK_{\delta C}, \tag{B2}$$

$$K_{\delta\beta_h/\beta_h} = 2NK_{\delta N}, \quad K_{\delta\beta_v/\beta_v} = 2LK_{\delta L} - 4L\eta K_{\delta F}, \tag{B3}$$

$$K_{\delta\eta/\eta} = FK_{\delta F}. \tag{B4}$$

The sensitivity kernels for relative perturbations of the isotropic  $P$ -wave speed  $\delta\alpha/\alpha$  and  $S$ -wave speed  $\delta\beta/\beta$  can be retrieved either from the Chen & Tromp kernels or from the wave speed kernels:

$$K_{\delta\alpha/\alpha} = 2\rho\alpha^2(K_{\delta A} + K_{\delta C} + K_{\delta F}) = K_{\delta\alpha_h/\alpha_h} + K_{\delta\alpha_v/\alpha_v}, \tag{B5}$$

$$K_{\delta\beta/\beta} = 2\rho\beta^2(K_{\delta L} + K_{\delta N} - 2K_{\delta F}) = K_{\delta\beta_h/\beta_h} + K_{\delta\beta_v/\beta_v}. \tag{B6}$$

### B2 Horizontal symmetry axis

Transverse isotropy with a horizontal symmetry axis is the model usually considered to interpret the azimuthal variations of surface-wave speeds or  $SKS$ -splitting measurements. Representing the mantle as a transversely isotropic medium with a horizontal symmetry axis, Favier & Chevrot (2003) analysed the sensitivity of the  $SKS$ -splitting intensity to two perturbation parameters  $\gamma_c$  and  $\gamma_s$ . These parameters are defined in terms of Thomsen's (1986) parameter  $\gamma$  representing  $S$ -wave anisotropy in transversely isotropic models. Eq. (16) of Chevrot (2006) writes the  $c_{ijkl}$  as functions of Thomsen's (1986) parameters and the coordinates of the symmetry axis. From this equation, and considering a symmetry axis lying in the horizontal plane with an azimuth of  $\xi_0$ , it is possible to derive the relations between Favier & Chevrot's (2003) parameters and the  $C_{IJ}$  or the Chen & Tromp parameters based upon the relations (A2). Only the transversely isotropic parameters ( $A$ ,  $C$ ,  $L$ ,

$N$  and  $F$ ) and the surface-wave parameters ( $B$ ,  $H$ ,  $G$  and  $E$ ) are involved in these relations. The body-wave parameters ( $J$ ,  $K$ ,  $M$  and  $D$ ) are zero in a transversely isotropic structure with a horizontal symmetry axis. We find that

$$G_c = -\rho\beta^2\gamma \cos 2\xi_0, \quad G_s = \rho\beta^2\gamma \sin 2\xi_0, \quad (\text{B7})$$

where we recognize Favier & Chevrot's (2003) parameters  $\gamma_c = \gamma \cos 2\xi_0$  and  $\gamma_s = \gamma \sin 2\xi_0$ . It is then possible to construct the kernels for Favier & Chevrot's (2003) parameters from the kernels for the Chen & Tromp parameters:

$$K_{\delta\gamma_c} = \rho\beta^2(2K_{\delta H_c} - K_{\delta G_c}), \quad K_{\delta\gamma_s} = -\rho\beta^2(2K_{\delta H_s} - K_{\delta G_s}). \quad (\text{B8})$$

Our experiments indicate that  $K_{\delta H} \simeq 0$  for the *SKS*-splitting intensity. We therefore, may write for this observable

$$K_{\delta\gamma_c} \simeq -\rho\beta^2 K_{\delta G_c}, \quad K_{\delta\gamma_s} \simeq \rho\beta^2 K_{\delta G_s}. \quad (\text{B9})$$

With these last relations, our results can be readily compared to Favier & Chevrot's (2003) analysis.